Chapter 24
Response of a Stratified Alpine Lake to External Wind Fields: Numerical Prediction and Comparison with Field Observations

List of Symbols

Roman Symbols

A_0	Constant momentum Austausch coefficient, horizontal momentum diffusivity
A_1	BENNETT's areal diffusivity $A_1 = \frac{1}{4}\Delta x \Delta y\, f$
$b(x, y) = z$	Equation for the lake bottom
$C(\|\boldsymbol{v}\|)$	Basal drag coefficient
c	Phase velocity
c_p	Specific heat at constant pressure
c_w	Wind drag coefficient
$\boldsymbol{D}$	Strain rate tensor, stretching tensor $\boldsymbol{D} = \frac{1}{2}(\text{grad}\,\boldsymbol{v} + \text{grad}\,\boldsymbol{v})^T$
div	Divergence operator
E	Total energy $E = PE + KE$
$f = 2\|\Omega\|\sin\phi$	First CORIOLIS parameter
$\tilde{f} = 2\|\Omega\|\cos\phi$	Second CORIOLIS parameter
$\boldsymbol{g}, g$	Gravity vector, gravity constant
grad	Gradient operator
h	Specific enthalpy
h_1, h_2	Epilimnion thickness, hypolimnion thickness
h_k	Thickness of the kth horizontal layer
k	Counting index
KE	Kinetic energy
M	Fourth order viscosity tensor
p	Pressure
PE	Potential energy

This chapter is greatly inspired by the report of Gordon OMAN [19] who, in 1981/1982 worked under the supervision of K.H. and wrote the referenced report in just one year's time. The concept of the report and all sweat which is connected with it is G.O's, but the German version of the text was designed by K.H. In this chapter we heavily draw from this report and quote often from it, now in the English language. The text is newly arranged and considerably shortened and where translated the interpretation is free and not word-by-word. We omit quotation marks and simply state that G.O's article is the source.

K. Hutter et al., *Physics of Lakes, Volume 3: Methods of Understanding Lakes as Components of the Geophysical Environment*, Advances in Geophysical and Environmental Mechanics and Mathematics,
DOI: 10.1007/978-3-319-00473-0_24, © Springer International Publishing Switzerland 2014

$\boldsymbol{Q}$	Heat flux vector
Q^{atm}	Atmospheric heat flow at the lake surface
$\boldsymbol{Q}^{\text{lam}}$	Laminar heat flux vector $\boldsymbol{Q}^{\text{lam}} = -\kappa \text{grad } T$
$\boldsymbol{Q}^{\text{turb}}$	Mean turbulent heat flux vector $\boldsymbol{Q}^{\text{turb}} = -\rho \langle c_p T' \boldsymbol{v}' \rangle$
$(Q_z)_{k+1/2}$	z component of the heat flux vector at the interface between layer k and $k+1$
R	ROSSBY radius (of deformation)
Ri	(Gradient) RICHARDSON number
s	Salinity, mineralization
$\hat{S}_k$	Buoyancy weight of the column above $z = z_{k+1/2}$ $\hat{S}_k \approx g \int_{z_{k+1/2}}^{0} \sigma(z) \mathrm{d}z$
T	Temperature (Celsius or Kelvin)
T^*	Reference temperature (4 °C)
T_k	Average temperature in layer k
T^{atm}	Atmospheric temperature at the lake surface
T_{base}	Temperature at the bottom of the lake
$\boldsymbol{T}$	CAUCHY stress tensor
$\boldsymbol{T}_E$	Extra CAUCHY stress tensor (deviator)
$\boldsymbol{T}'$	Fluctuation of $\boldsymbol{T}$
$\boldsymbol{T}_E^{\text{turb}}$	Mean turbulent CAUCHY stress deviator $\boldsymbol{T}_E^{\text{turb}} \equiv \langle \rho \boldsymbol{v}' \otimes \boldsymbol{v}' - \frac{1}{3} \text{tr}(\rho \boldsymbol{v}' \otimes \boldsymbol{v}') \boldsymbol{1} \rangle$
$\boldsymbol{T}_E^{\text{lam}}$	Laminar CAUCHY stress
T_{ij}	Components of $\boldsymbol{T}$ $((i, j = 1, 2, 3))$
$t_x^{\text{wind}}, t_y^{\text{wind}}$	Shear traction components of the wind stress at the lake surface
tr	Trace operator
$\boldsymbol{t}_\vert$	Tangential shear traction at the bottom surface
u, v, w	Cartesian components of the velocity vector
u_k, v_k	Average horizontal velocity components in layer k
$\boldsymbol{v}$	Velocity vector
$\boldsymbol{v}'$	Turbulent velocity fluctuation
$\boldsymbol{v}_\vert$	Tangential water velocity vector at the bottom surface
$\boldsymbol{W}$	Wind velocity
$w_{k+1/2}$	Vertical velocity at the interface between layers k and $k+1$
x, y, z	Cartesian coordinates

Greek Symbols

$\Delta\rho$	Density difference $\rho_2 - \rho_1, \rho_2 > \rho_1$
$\Delta x, \Delta y, \Delta z$	Side lengths of the finite difference grid
φ	Angle of geographical latitude
$\boldsymbol{\kappa}, \kappa$	Tensor of heat conductivity, heat conductivity
κ_v	Vertical heat conductivity
ν	Kinematic viscosity
ν_v	Vertical kinematic viscosity
ρ	Density of water $\rho = \rho(T, p, s)$
ρ_0	Reference density ($\rho = \rho(T \approx 30\,°\text{C})$)
$\sigma = (\rho/\rho_0 - 1)$	Density anomaly
$\zeta(x, y, t) = z$	Free surface displacement
$\boldsymbol{\Omega}$	Angular velocity of the Earth

The water motion in lakes during summer stratification is primarily generated by wind. It is chiefly influenced by the vertical density distribution, which leads to a strong interplay between the direct circulation dynamics and internal oscillations. In a storm-type wind set-up from rest the on-setting circulation flow also causes the formation of internal seiches, which, according to observations in numerous mountainous lakes [12], persist for several periods after wind cessation. On the basis of the hydrostatic and BOUSSINESQ-approximated baroclinic non-linear hydrodynamic model, which is discretized by a multi-layered finite difference description, the baroclinic response of Lake Zurich to such a stormy scenario is predicted and compared with an episode, which was observed in Lake Zurich in a summer field campaign in 1978. A careful parameter study shows that the model appears to predict direct wind driven response in a qualitatively correct manner. It also correctly predicts the formation and propagation of internal temperature surges characterized by an extremely fast falling thermocline. However, it seems to suffer from an excessive dissipation of energy, which causes the internal seiche to oscillate too slowly and die out too quickly. This loss of energy can be attributed to numerical diffusion of the temperature, which is needed to prevent convective instability in the model and avoid large dissipation of kinetic energy caused by the horizontal smoothing of the velocity field needed to control unrealistically large oscillations of the vertical component of velocity. Decreasing vertical eddy viscosity and increasing the vertical resolution near the thermocline reduces but does not eliminate this energy dissipation, some of which appears necessary to assure model stability.

24.1 The Problem Setting

The water motion in lakes is primarily caused by wind, which by its shear stresses at the free surface provides a persistent momentum flow from the atmosphere into the lake. These motions can mathematically be described by field equations, which are deduced from the NAVIER–STOKES equations by imposing the simplifying assumptions of BOUSSINESQ and hydrostatic pressure. Under stratified conditions two classes of dynamic behavior exist, the *barotropic* and *baroclinic* responses, of which the second comprises the dominant motion during the summer months and in autumn when strong vertical density gradients prevail. Barotropic current distributions have been studied for Lake Zurich in Chap. 23; the baroclinic response of Lake Zurich to impulsive wind scenarios is the focus of this chapter. We study the response of the Lake Zurich currents and fathom the conditions how observed behavior can best be reproduced by model computations. This scrutinizing analysis follows a remote report by OMAN of 1982 [19].

Lake Zurich is of narrow longitudinal form with a thalweg length of approximately 28 km and a maximum width of about 4 km. It is naturally separated into two basins by a glacially formed sill, the ‘lower lake’ and the ‘upper lake’ (Obersee), see Fig. 24.1. The two basins are connected by an opening of the dam at Rapperswil (situated at the upper end of the lower lake), which is so small that the two basins are dynamically

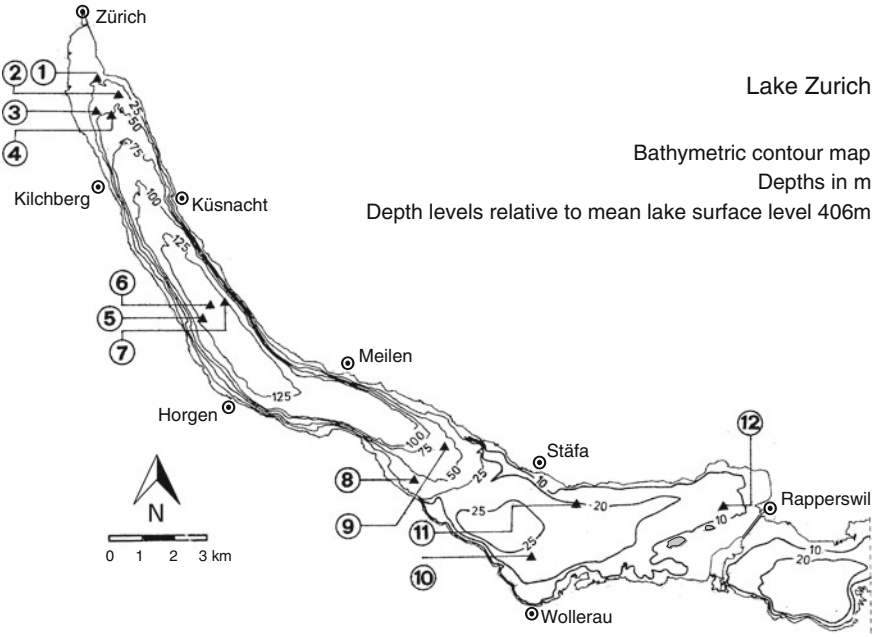


Fig. 24.1 Lake Zurich map, showing 12 positions, labeled [(1)] to [(12)], where current meters, thermistor chains and meteorological buoys [(4)], [(6)], [(11)], were moored in a field experiment in August/September 1978. The two islands in the upper portion of the lower lake are called Ufenau and Lützelau © Versuchsanstalt für Wasserbau, Hydrologie und Glaziologie an der ETH Zürich, reproduced with permission

uncoupled. Subsequently, we shall restrict considerations to the lower lake and will refer to it as Lake Zurich. The deeper and larger part of this basin has a maximum depth of 136 m and extends to northwest, with the upper end at Rapperswil and the lower end at Zurich. The more shallow and broader, eastern part extends towards west; with its depth of 22 m it connects the deeper part of the basin by a relatively steep transition zone of 3 % mean inclination between Meilen and Stäfa. The mean depth and mean width of the lake are 51 m and 2.4 km, respectively, and the free surface area of the lower lake relative to 406 m a.s.l. is 67 km^3. The main tributary to the lake is the river Lindt (entering the upper lake) with approximately 50 $m^3 s^{-1}$ discharge. Other, smaller, tributaries contribute approximately the same amount. The exit is the river Limmat at Zurich with a mean discharge of approximately 100 $m^3 s^{-1}$. The mean residence time of the water is therefore between 1 and 2 years. The outflow is monitored by a weir, a few 100 m below the exit cross section; long-term fluctuations of the water level are therefore small, in general.

It is suspected that the relatively complex form and bathymetry of the lake exerts a decisive influence to the wind-induced motion of Lake Zurich. To clarify this, and in particular to correlate the current and density fields, which the driving forces (wind, atmospheric pressure) induce, a field experiment was conducted in 1978 by the Laboratory of Hydraulics, Hydrology and Glaciology at ETH Zurich, in which

at 11 positions current meters and thermistor chains (with 11 thermistors, generally at 2 meters distances) were mounted, see Fig. 24.1; a single current meter was also deployed at positions [1] and [12], and at positions [4], [6] and [11] meteorological buoys were erected, which measured wind, atmospheric pressure and solar radiation.[1]

We refer to this exploratory work insofar as its results are necessary for the verification of the numerical model. The persistent oscillations of the water temperature, particularly in the metalimnion, can be viewed as a typical sign of the temperature registrations. These oscillations in the measurements of Lake Zurich manifest themselves mainly with periods of approximately 45 and 24 h and last, once induced by the wind, in many episodes over several periods, see [3, 4, 17]. The existence of these internal oscillations can first be traced back to the fact that relevant wind episodes are of shorter duration than the period of the fundamental internal seiche and, second, that they are sufficiently strong to trigger the internal oscillations. It is a typical characteristic behavior of stratified Lake Zurich that after wind cessation both the current and temperature fields oscillate with only relatively small attenuation.

If a numerical software package is expected to model current and temperature evolutions in a lake correctly for time intervals which lie within the temporal scale of the periods of internal oscillations and encompass several days to weeks, then we must request that this model generates not only the water velocity and temperature distributions during simultaneous wind action with sufficient accuracy, but also reproduces these ensuing fields after wind cessation. We shall see that with the present numerical model the processes after wind cessation can hardly be adequately reproduced. This result is unique, because comparison of numerical models focusing on baroclinic processes in lakes with whole lake synoptic field campaigns other than this one are not known to us.

The fundamental equations of the atmospherically driven currents in stratified lakes or oceans are the balance laws of mass, momentum and energy, which we shall use in the BOUSSINESQ and hydrostatic pressure approximations. These equations will be integrated by exploring a discretization based on finite differences. Explicitly, the region of integration, i.e., the lake domain will be divided into layers with spatially fixed horizontal interfaces. In each layer, depth averaging is performed; this transforms the original three-dimensional problem for the entire lake into a system of two-dimensional problems for the layers, which are being solved by the finite difference method. Exchange of momentum and heat (i.e., REYNOLDS stresses and heat fluxes) are parameterized by 'gradient-type relations' involving viscosity and diffusion coefficients in the horizontal and vertical directions. However, because of reasons of numerical stability these coefficients need on occasion be enlarged, and the amount of this numerical diffusion depends on the spatial and temporal discretization steps. The smaller these discretization increments are, the smaller will be the necessary numerical diffusion for stable performance of the integration procedure of the equations. The addition of artificial numerical diffusion also distorts the numerical results of the physical processes and, if it is excessively large, mechanical energy will be destroyed and, as a consequence, oscillations will be strongly attenuated.

[1] This campaign has been scientifically explored by the following reports: [4–7, 16, 17, 19].

If the numerical diffusion is not large enough, unphysical instabilities may develop, which trigger (mostly other) unwanted oscillations or generate strong unphysical growth of some variables. The difficulty is to find the conditions under which numerical stability prevails and the physics is not unduly falsified. This mostly leads to statements of constraints of physical processes for which the numerical scheme can be judiciously applied.

The above text outlines the focus of the present chapter. In ensuing sections the basic three-dimensional boundary value problem will be formulated, transformed into a set of layered equations, and the numerical discretization will briefly be outlined. Test runs concern the stratified Lake Zurich subject to an impulsively applied wind from *west*, spatially uniform and constant in time for one day with instant inception and equally abrupt cessation. We search for conditions under which the current and temperature fields are quantitatively correctly reproduced during the 24 h of active wind and during the days after wind cessation. Somewhat simplified, the result is: As long as the relatively uniform wind is exerted, the computation delivers reliable distributions of the water currents and temperature. However, the water motion after wind cessation is not satisfactorily reproduced. Using the optimal parameterizations for numerical diffusion and a discretization with 18 layers, a post Föhn-storm event is computed which compares reasonably but still not completely satisfactorily with the data from the 1978 field campaign.

24.2 Governing Equations

24.2.1 Field Equations for a Boussinesq Fluid

The governing equations for the fluid transport and temperature distributions in a lake under summer stratification are the turbulent equations of balances of mass, momentum and energy subject to laminar viscous, heat conducting and corresponding turbulent closure conditions. In the BOUSSINESQ approximation density variations are ignored everywhere except in the gravity force. When the turbulent fluctuating motion is taken into account these REYNOLDS averaged equations are as follows:

$$\begin{aligned}
&\text{mass balance } \operatorname{div} \boldsymbol{v} = 0,\\
&\text{momemtum balance } \rho \frac{\mathrm{d}\boldsymbol{v}}{\mathrm{d}t} = -\operatorname{grad}\ p + \operatorname{div} \boldsymbol{T}_E + \rho \boldsymbol{g} - \rho(2\boldsymbol{\Omega} \times \boldsymbol{v}), \qquad (24.1)\\
&\text{energy balance } \rho \frac{\mathrm{d}h}{\mathrm{d}t} - \frac{\mathrm{d}p}{\mathrm{d}t} = -\operatorname{div} \boldsymbol{Q} + \operatorname{tr}(\boldsymbol{T}_E \cdot \boldsymbol{D}),
\end{aligned}$$

in which ρ, $\boldsymbol{v}$, p, $\boldsymbol{T}_E$, $\boldsymbol{g}$, h, $\boldsymbol{Q}$ are the mass density, velocity vector, pressure, CAUCHY stress deviator, gravity acceleration vector, specific enthalpy and heat flux vector, respectively. Moreover,

$$\boldsymbol{D} = \operatorname{sym} \operatorname{grad} \boldsymbol{v} = \tfrac{1}{2}\left(\operatorname{grad} \boldsymbol{v} + \operatorname{grad}^T \boldsymbol{v}\right), \qquad (24.2)$$

in which $\boldsymbol{A}^T$ is the transpose of the matrix $\boldsymbol{A}$ and tr$(\cdot)$ is the trace operator. For not too deep lakes of less than 500 m depth the term $-\mathrm{d}p/\mathrm{d}t$ is generally ignored; this will also be done here.

The last term in $(24.1)_2$ is the contribution of the CORIOLIS force; $\boldsymbol{\Omega}$ is the angular velocity of the Earth with the components $\boldsymbol{\Omega} = (0, \|\boldsymbol{\Omega}\| \cos\varphi, \|\boldsymbol{\Omega}\| \sin\varphi)$ in a Cartesian coordinate system, x (east), y (north) and z (zenith) and φ the geographical latitude, implying

$$2\boldsymbol{\Omega} \times \boldsymbol{v} = \Big(\tilde{f} w - f v, f u, -\tilde{f} u\Big), \quad f \equiv 2\|\boldsymbol{\Omega}\| \sin\varphi, \quad \tilde{f} \equiv 2\|\boldsymbol{\Omega}\| \cos\varphi. \tag{24.3}$$

Closure relations are formulated for $\boldsymbol{T}_E$, $\boldsymbol{Q}$, h and are given here as

$$\begin{aligned} \boldsymbol{T}_E &= \boldsymbol{T}_E^{\mathrm{turb}} + \boldsymbol{T}_E^{\mathrm{lam}} = -\langle \rho(\boldsymbol{v}' \otimes \boldsymbol{v}' - \tfrac{1}{3}(\mathrm{tr}\boldsymbol{v}' \otimes \boldsymbol{v}')\mathbf{1})\rangle + \rho\nu \boldsymbol{D}, \\ \boldsymbol{Q} &= \boldsymbol{Q}^{\mathrm{turb}} + \boldsymbol{Q}^{\mathrm{lam}} = -\rho\langle c_p T' \boldsymbol{v}'\rangle - \kappa\, \mathrm{grad}\ T, \\ h &= c_p(T - T^*). \end{aligned} \tag{24.4}$$

T is the KELVIN or CELSIUS temperature and primes indicate turbulent fluctuations, whilst $\langle\cdot\rangle$ signifies turbulent averages of the turbulent correlation terms. On the other hand, ν, κ, c_p are the kinematic viscosity, the heat conductivity and the specific heat at constant pressure for water. In writing down (24.4) it was further assumed that the water behaves as a linearly viscous fluid (attributed to NAVIER-STOKES with kinematic viscosity ν, that the heat flux vector is given by the FOURIER relation $Q_\ell = -\kappa \mathrm{grad}\ T$ with constant heat conductivity and that the enthalpy function is a linear function of the temperature with specific heat c_p and $T^* = 273.15$ K. This linear representation is sufficiently accurate for $T \in [273.15, 305]$ K. The parameterizations $(24.4)_{1,2}$ represent compositions of turbulent and laminar contributions $\boldsymbol{T}_E = \boldsymbol{T}_E^{\mathrm{turb}} + \boldsymbol{T}_E^{\mathrm{lam}}$, $\boldsymbol{Q} = \boldsymbol{Q}^{\mathrm{turb}} + \boldsymbol{Q}^{\mathrm{lam}}$. The former have not yet been parameterized. This will be done later.[2]

The above equations do not explicitly make visible that the BOUSSINESQ assumption is imposed. This has been done implicitly by replacing the exact balance of mass equation

$$\frac{\mathrm{d}\rho}{\mathrm{d}t} + \rho \mathrm{div}\, \boldsymbol{v} = 0 \quad \text{by} \quad \mathrm{div}\, \boldsymbol{v} = 0, \tag{24.5}$$

even though ρ may vary with temperature and pressure. Moreover, everywhere in (24.1)–(24.4) ρ is interpreted as a constant $\rho^* = \rho(T^*)$, which is the density at normal pressure and at 277.15 K (4 °C), except in the gravity term $\rho\boldsymbol{g}$. This means that, kinematically, the mathematical fluid is density preserving (and the velocity field is solenoidal), but the buoyancy effects of the gravity force are taken into account. Strictly, in the terms on the left-hand side of $(24.1)_{2,3}$ ρ is replaced by ρ^*; however,

[2] Note that $\boldsymbol{T}_E^{\mathrm{turb}}$ consists of two contributions, of which the second, $-\frac{1}{3}\mathrm{tr}(\langle(\boldsymbol{v}' \otimes \boldsymbol{v}')\rangle)\mathbf{1}) \equiv k$ is the turbulent kinetic energy, which we have subtracted from $\langle(\boldsymbol{v}' \otimes \boldsymbol{v}')\rangle$ to make $\boldsymbol{T}_E^{\mathrm{turb}}$ a deviator. The contribution of the turbulent kinetic energy is absorbed in the pressure term!

in a loose interpretation of the BOUSSINESQ approximation the variability of ρ in the sense that $\rho = \rho(T, p)$ may only be dropped in the continuity equation. This then means that the essential assumption of the BOUSSINESQ approximation is to make the water-velocity field solenoidal or to eliminate acoustic wave signals. Subsequently, we will use the strong BOUSSINESQ approximation.

24.2.2 The Hydrostatic Approximation of the Boussinesq-Type Field Equations

If internal wave breaking and strong up- and downwelling are ignored and inversions of the density stratification can be excluded as possible processes, then the shallowness assumption can be supposed to be valid. In this assumption the horizontal length and velocity scales are large in comparison to their vertical counterparts. It then follows that the vertical momentum balance reduces to $\partial p/\partial z = -\rho\, g$ or after an integration in z

$$p(z) = \int_{\bar{z}=z}^{\bar{z}=\zeta} \rho\, g \mathrm{d}\bar{z} + p^{\mathrm{atm}}(x, y, t). \tag{24.6}$$

Here, $z = \zeta(x, y, t)$ is the vertical displacement of the free surface from its equilibrium position. Physically interpreted, this says that the pressure at depth z (below the undeformed free surface) is the sum of the atmospheric pressure, p^{atm} at the free surface plus the weight of the water column above z. If we now write $\rho = \rho + \rho_0 - \rho_0$, where $\rho_0 \approx \rho(300K)$, (i.e., the highest temperature in the lake water), then (24.6) can, alternatively be written as

$$p(z) = \rho_0\, g(z - \zeta) + \rho_0 g \int_{\bar{z}=z}^{\bar{z}=\zeta} \sigma \mathrm{d}\bar{z}, \quad \sigma = \left(\frac{\rho}{\rho_0} - 1\right). \tag{24.7}$$

σ is called the density anomaly, which is generally a function of temperature and (for deep lakes) the pressure $\sigma = \sigma(T, p)$.

The pressure function (24.7) can be differentiated with respect to x and y, and the result can then be substituted into the horizontal components of the momentum equations. When in the energy equation also the power of working of the stress deviator, $\mathrm{tr}(\boldsymbol{T}_E \boldsymbol{D})$ is ignored, the approximate field equations take the forms

$$\begin{aligned}
&\frac{\partial u}{\partial x} + \frac{\partial v}{\partial y} + \frac{\partial w}{\partial z} = 0,\\
&\left(\frac{\partial u}{\partial t} + \frac{\partial u^2}{\partial x} + \frac{\partial uv}{\partial y} + \frac{\partial uw}{\partial z}\right) = -g\frac{\partial \zeta}{\partial x} - \frac{1}{\rho_0}\frac{\partial p^{\mathrm{atm}}}{\partial x} - \frac{\partial}{\partial x}\int_z^\zeta g\,\sigma\, \mathrm{d}\bar{\zeta},\\
&\qquad\qquad + \frac{1}{\rho_0}\left(\frac{\partial T_{xx}}{\partial x} + \frac{\partial T_{xy}}{\partial y} + \frac{\partial T_{xz}}{\partial z}\right) + f\, v,
\end{aligned} \tag{24.8}$$

$$\left(\frac{\partial v}{\partial t}+\frac{\partial vu}{\partial x}+\frac{\partial v^2}{\partial y}+\frac{\partial vw}{\partial z}\right)=-g\frac{\partial \zeta}{\partial y}-\frac{1}{\rho_0}\frac{\partial p^{\mathrm{atm}}}{\partial y}-\frac{\partial}{\partial y}\int_z^\zeta g\,\sigma\,\mathrm{d}\bar{\zeta},$$
$$+\frac{1}{\rho_0}\left(\frac{\partial T_{xy}}{\partial x}+\frac{\partial T_{yy}}{\partial y}+\frac{\partial T_{yz}}{\partial z}\right)-f\,u,$$
$$\left(\frac{\partial T}{\partial t}+\frac{\partial uT}{\partial x}+\frac{\partial vT}{\partial y}+\frac{\partial wT}{\partial z}\right)=\frac{1}{\rho_0 c_p}\left(\frac{\partial Q_x}{\partial x}+\frac{\partial Q_y}{\partial y}+\frac{\partial Q_z}{\partial z}\right),$$

in which the shallow water approximation of the CORIOLIS force is reduced to the contributions $2\boldsymbol{\Omega}\times\boldsymbol{v}\approx(-fv,\,fu,\,0)$, see Vol. I, Chap. 4, Sect. 4.7, pp. 150–152. We have also dropped the index $(\cdot)_E$ in the stress deviator components T_{xx}, ..., T_{yz} and will do this henceforth consistently.

24.2.3 Turbulent Closure Conditions

Equations (24.8) need to be complemented by closure relations for the stress components T_{xx}, ..., T_{yz} and the turbulent heat flux components Q_x, Q_y, Q_z. This has been done by OMAN [19] in the most simple way by assuming that $\boldsymbol{T}$ is linearly related to $\boldsymbol{D}$ and $\boldsymbol{Q}$ is linearly related to grad T as

$$\boldsymbol{T}=\mathsf{M}\boldsymbol{D},\qquad \boldsymbol{Q}=-\boldsymbol{\kappa}\,\mathrm{grad}\;T, \tag{24.9}$$

in which $\boldsymbol{T}$, $\boldsymbol{D}$, $\boldsymbol{Q}$ and T are averaged turbulent fields, M is a fourth order viscosity tensor and $\boldsymbol{\kappa}$ a second order tensor of heat conduction. It is assumed that turbulent diffusion of momentum and heat are different in distinct directions of the space; in limnology, meteorology and oceanography it is supposed that the dominant differences of turbulent diffusion are in the horizontal and vertical directions. This transversely isotropic turbulence assumption, first postulated by MUNK in 1950 [18] and when expressed in the stress and heat flux divergence terms take the forms

$$\begin{aligned}
\frac{\partial T_{xx}}{\partial x}+\frac{\partial T_{xy}}{\partial y}&=\rho_0 A_0\Delta\,u,\quad \frac{\partial T_{xz}}{\partial z}=\frac{\partial}{\partial z}\left(\rho_0\,\nu(z)\frac{\partial u}{\partial z}\right),\\
\frac{\partial T_{yx}}{\partial x}+\frac{\partial T_{yy}}{\partial y}&=\rho_0 A_0\Delta\,v,\quad \frac{\partial T_{yz}}{\partial z}=\frac{\partial}{\partial z}\left(\rho_0\,\nu(z)\frac{\partial v}{\partial z}\right),\\
\frac{1}{\rho_0 c_p}\left(\frac{\partial Q_x}{\partial x}+\frac{\partial Q_y}{\partial y}\right)&=\kappa_h\Delta\,T,\quad \frac{1}{\rho_0 c_p}\frac{\partial Q_z}{\partial z}=\frac{\partial}{\partial z}\left(\kappa_v(z)\frac{\partial T}{\partial z}\right),
\end{aligned} \tag{24.10}$$

in which

$$\Delta=\frac{\partial^2}{\partial x^2}+\frac{\partial^2}{\partial y^2}$$

is the horizontal LAPLACE operator and A_0 and κ_h are horizontal exchange coefficients which can be treated as constants; $\nu(z)$ and $\kappa_v(z)$ are the vertical exchange

coefficients of momentum and heat, both with dimensions $[m^2 s^{-1}]$. Their values in the epilimnion and hypolimnion are considerably different from one another, see e.g. [10, 19].

A justification of the closure relations (24.10) is not easy, in fact, based on strict objectivity arguments, it is not possible. An attempt of delineating the near correctness of (24.10) has been given by WANG [28] and is reproduced in Vol. I, Chap. 6, pp. 212–219.

24.2.4 Boundary Conditions

Integration of the field Eqs. (24.8), (24.10) requires formulation of boundary conditions at the free surface and the bed.

- At the free surface, defined by the equation $z = \zeta(x, y, t)$, the kinematic boundary condition

$$\frac{\partial \zeta}{\partial t} + \frac{\partial \zeta}{\partial x} u + \frac{\partial \zeta}{\partial y} v - w = 0 \tag{24.11}$$

  forms an evolution equation for the free surface displacement ζ. This equation is complemented by the dynamic requirement that the surface traction is continuous across the material interface. This condition says that $p = p^{\text{atm}}$ and $(\boldsymbol{T} - (\boldsymbol{n} \cdot \boldsymbol{T}\boldsymbol{n})\mathbf{1})\,\boldsymbol{n} = \boldsymbol{t}^{\text{wind}}$. Since the length scales of atmospheric pressure variations are generally much larger than the horizontal extent of the lake, p^{atm} can be treated as a constant, which without loss of generality can be set to zero. On the other hand, continuity of the shear traction across the surface implies $T_{xz} = t_x^{\text{wind}}$ and $T_{yz} = t_y^{\text{wind}}$. With (24.10) the stress boundary conditions at the free surface are thus given by

$$p = p^{\text{atm}}, \quad \rho_0 \nu(0) \frac{\partial u}{\partial z} = t_x^{\text{wind}} \quad \rho_0 \nu(0) \frac{\partial v}{\partial z} = t_y^{\text{wind}}. \tag{24.12}$$

  Strictly, these conditions apply at the deformed free surface, however, because free surface displacements are small, they hold with sufficient accuracy on the undeformed surface $z = 0$. This simplifies their incorporation in the computational scheme.
  Finally, we must add a parameterization of the wind shear stress $\boldsymbol{t}^{\text{wind}}$, which will be given here as [27, 28]

$$\boldsymbol{t}^{\text{wind}} = \rho\, c_w \| \boldsymbol{W} \| \boldsymbol{W}, \tag{24.13}$$

  where $\boldsymbol{W}$ is the wind velocity, generally measured 10 m above the water surface. The drag coefficient c_w depends on the height at which $\boldsymbol{W}$ is measured and also on the surface roughness and the fetch. Numerical values are given by LASKA (1981) [13]
- As was done for the free surface the basal surface is material but it is also immobile. So, $z = b(x, y)$ is known once and for all. Of course, this assumes that no sediment transport occurs. As for the dynamic boundary condition a sliding law is employed.

It relates the tangential traction to the tangential velocity

$$\underbrace{(\boldsymbol{T} - (\boldsymbol{n} \cdot \boldsymbol{T}\boldsymbol{n})\mathbf{1})\,\boldsymbol{n}}_{\boldsymbol{t}_\parallel} = \rho_0 C(\|\boldsymbol{v}\|)\,\underbrace{(\boldsymbol{v} - (\boldsymbol{n} \cdot \boldsymbol{v})\boldsymbol{n})}_{\boldsymbol{v}_\parallel} = \rho_0 C(\|\boldsymbol{v}\|)\boldsymbol{v}_\parallel, \tag{24.14}$$

in which $C(\|\boldsymbol{v}\|)$ is a sliding speed-dependent drag coefficient. The limit values $C \to 0$ and $C \to \infty$ correspond to a frictionless boundary ($\boldsymbol{t}_\parallel = \mathbf{0}$) and no-slip condition ($\boldsymbol{v} = \mathbf{0}$). Because $\boldsymbol{v} \cdot \boldsymbol{n} = 0$ at the rigid bed, the expression on the far right-hand side of (24.14) is equally valid. In Cartesian coordinates and with the shallowness assumption $\|\partial H/\partial x\|, \|\partial H/\partial y\| \ll 1$, (24.14) can also be written as

$$T^b_{xz} = \rho_0 C(\|\boldsymbol{v}\|)u, \quad T^b_{yz} = \rho_0 C(\|\boldsymbol{v}\|)v, \quad \text{at } z = b(x, y). \tag{24.15}$$

Usual parameterizations for C are linear in $\|\boldsymbol{v}\|$, so, see [1, 2, 13, 25]

$$C(\|\boldsymbol{v}\|) = c_b\|\boldsymbol{v}\|, \quad c_b = 0.002. \tag{24.16}$$

To summarize, the boundary value problem is described by the field Eqs. (24.8), (24.10), the free surface boundary conditions (24.11), (24.13) and the basal boundary conditions at the basal surface (24.15) and (24.16).

24.3 Approximate Treatments of the Model Equations

24.3.1 Discretization Procedure

The governing equations for the determination of the velocity and temperature distributions in stratified lakes are prepared in this chapter for the application of their numerical integration. We shall employ the finite difference method (FDM); its formulation was laid down by SIMONS [21–25] and LEENDERTSE et al. [14, 15] and was adopted to Lake Zurich by OMAN [19].

The finite difference grid follows a Cartesian coordinate system x, y, z, where x, y are 45 °C rotated from the east-west and south-north directions and z is vertical against gravity. The net is adjusted to optimally approximate the lake shore by line segments parallel to the x- and y-axes; its choice also depends on the selection of the side lengths $\Delta x, \Delta y, \Delta z$, of the quadrilateral elements, Fig. 24.3. The unknown field variables are determined at the grid points of the net. The initial boundary value problem, expressed by differential equations and boundary conditions is then transformed into an algebraic system of equations; the integration is thus replaced by solving algebraic equations. There are several possibilities to define nodal values of the unknown variables—at the intersections of the grid, the midpoints of the element surfaces and of the element centres. The choice influences the accuracy and numerical stability of the numerical scheme, but, optimal choices are well known.

(a)



(b)

Big whirls have little whirls that feed on their velocity,
and little whirls have lesser whirls and so on to viscosity

Fig. 24.2. a Lewis Fry RICHARDSON, D. Sc. FRS, *11. 11. 1881, New Castle upon Tyne, † 30. 09 1953 Kilmun, Argyll and Bute. **b** Verse published in *Weather Prediction by Numerical Process* (p. 66)

L. F. RICHARDSON was a famous mathematician, physicist, mete orologist, psychologist and pacifist, who pioneered modern mathematical techniques of weather forecasting and the application of similar techniques to studying the causes of wars and how to prevent them. He is also known for pioneering work on fractals and a method of solving linear equations, known as modified RICHARDSON iteration.

As a Quaker, RICHARDSON's beliefs entailed an ardent pacifism that made him a conscientious objector of any war and war related work. This disqualified him from having any academic post throughout his life and forced him several times to change his positions and research foci. RICHARDSON's interest in meteorology caused him to propose a scheme for weather forecasting by solution of differential equations, nowadays routinely used by electronic computing, but not yet available during 1922. He was also interested in atmospheric turbulence and performed many terrestrial experiments. The RICHARDSON number, a measure of stability/instability transition from laminar to turbulent stratified flows is named after him. He famously summarized turbulence in the rhyming verse (stated above).

RICHARDSON's most celebrated achievement is his retroactive attempt to forecast the weather during a single day—20 May 2910—by direct computation. His prediction failed miserably, but it was found out much later, that the cause was a failure to apply smoothing techniques to the data, which in this case rules out unphysical surges of pressure. When these are applied, the forecast was accurate. RICHARDSON also performed work on the length of the border line between neighbouring countries and the echolocation of ice bergs, thus anticipating modern studies on fractals and the invention of sonars.

Figure and text based on: http://en.wikipedia.org/wiki/Lewis_Fry_Richardson

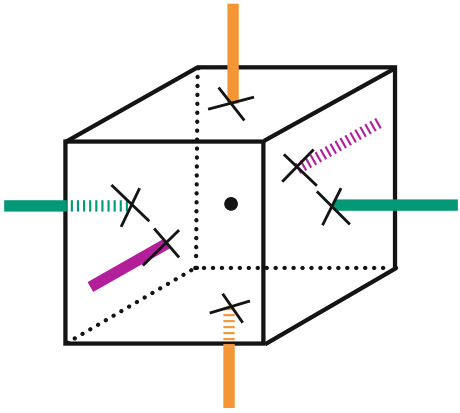


Fig. 24.3 Isolated element from a finite difference net. In the centre, density ρ, temperature, T and pressure, p, identified by •, are defined, in the mid points of the side surfaces those velocity components which are orthogonal to the respective surface are defined as indicated by the coloured segments

Most finite difference methods applied to the above system of equations employ a so-called RICHARDSON[3] net as indicated in Fig. 24.3. Density ρ, temperature T and pressure p are defined in the element centres, whilst the midpoints of the six side surfaces are reserved for the representation of the velocity components normal to them. This net allows second order approximation of spatial derivatives of unknown variables in the side lengths Δx, Δy, Δz. Second order approximations in time are achieved here by iterative and implicit integration techniques.

24.3.2 The Baroclinic Multi-Layer Model

A first step in the development of a discretized version of Eq. (24.8) is the division of the lake into a number of horizontal layers with immobile interfaces. A schematic sketch is given in Fig. 24.4. Density, velocity and temperature within single layers are assumed to be uniform in depth but variable in the horizontal direction. Equations (24.8), (24.10) are integrated over the depths of the layers by accounting for the transition conditions at the interfaces. This integration is straightforward if somewhat long. A detailed derivation can be made by the reader himself/herself or [25] may be consulted. With the definitions of the mean velocity components (u_k, v_k) and temperature T_k of the kth layer

[3] For a short biography of RICHARDSON see Fig. 24.2.

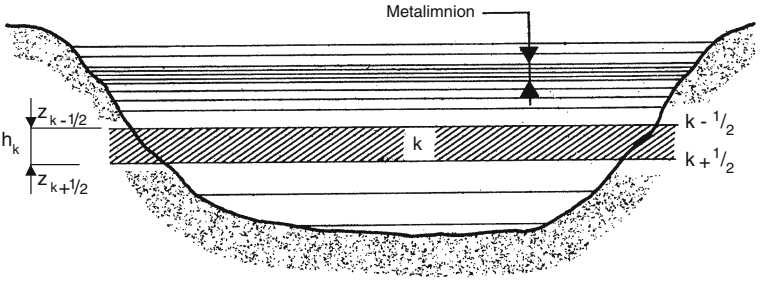


Fig. 24.4 Division of a lake into fixed horizontal layers. The interfaces between the layers are identified as $k + 1/2$ ($k = 1, 2, \ldots$) and the layers are identified by the index k

$$\begin{aligned}
\int_{-z_{k+1/2}}^{-z_{k-1/2}} u(z)\mathrm{d}z &= h_k u_k, \\
\int_{-z_{k+1/2}}^{-z_{k-1/2}} v(z)\mathrm{d}z &= h_k v_k, \qquad h_k = z_{k+1/2} - z_{k-1/2}, \\
\int_{-z_{k+1/2}}^{-z_{k-1/2}} T(z)\mathrm{d}z &= h_k T_k,
\end{aligned} \tag{24.17}$$

the continuity equation reads

$$\frac{\partial}{\partial x}(h_k u_k) + \frac{\partial}{\partial y}(h_k v_k) + (w_{k-1/2} - w_{k+1/2}) = 0, \tag{24.18}$$

and the horizontal momentum equations become

$$\begin{aligned}
&\frac{\partial}{\partial t}(h_k u_k) + \frac{\partial}{\partial x}\left(h_k u_k^2\right) + \frac{\partial}{\partial y}(h_k u_k v_k) + (u_{k-1/2} w_{k-1/2} - u_{k+1/2} w_{k+1/2}) \\
&= -g h_k \frac{\partial \zeta}{\partial x} - \frac{1}{\rho_0} h_k \frac{\partial p^{\mathrm{atm}}}{\partial x} - h_k \frac{\partial \hat{S}_k}{\partial x} + f\, h_k\, v_k \\
&\quad + A_0 \left[\frac{\partial^2}{\partial x^2}(h_k u_k) + \frac{\partial^2}{\partial y^2}(h_k u_k)\right] + \frac{1}{\rho_0}(T_{xz})_{k-1/2} - \frac{1}{\rho_0}(T_{xz})_{k+1/2}\,,
\end{aligned} \tag{24.19}$$

$$\begin{aligned}
&\frac{\partial}{\partial t}(h_k v_k) + \frac{\partial}{\partial x}(h_k u_k v_k) + \frac{\partial}{\partial y}\left(h_k v_k^2\right) + (v_{k-1/2} w_{k-1/2} - v_{k+1/2} w_{k+1/2}) \\
&= -g h_k \frac{\partial \zeta}{\partial y} - \frac{1}{\rho_0} h_k \frac{\partial p^{\mathrm{atm}}}{\partial y} - h_k \frac{\partial \hat{S}_k}{\partial y} - f\, h_k\, u_k \\
&\quad + A_0 \left[\frac{\partial^2}{\partial x^2}(h_k v_k) + \frac{\partial^2}{\partial y^2}(h_k v_k)\right] + \frac{1}{\rho_0}\left(T_{yz}\right)_{k-1/2} - \frac{1}{\rho_0}\left(T_{yz}\right)_{k+1/2}\,,
\end{aligned}$$

whilst the energy (heat) equation takes the form

$$\frac{\partial}{\partial t}\left(h_k T_k\right)+\frac{\partial}{\partial x}\left(h_k u_k T_k\right)+\frac{\partial}{\partial y}\left(h_k v_k T_k\right)+T_{k-1/2}w_{k-1/2}-T_{k+1/2}w_{k+1/2}$$
$$=\kappa_h\left[\frac{\partial^2}{\partial x^2}\left(h_k T_k\right)+\frac{\partial^2}{\partial y^2}\left(h_k T_k\right)\right]+\frac{1}{\rho_0 c_p}\left[\left(Q_z\right)_{k-1/2}-\left(Q_z\right)_{k+1/2}\right]. \quad (24.20)$$

In these equations the interior pressure is defined as

$$\hat{S}_k = g\int_{z_{k+1/2}}^{\zeta}\sigma(z)\mathrm{d}z \approx g\int_{z_{k+1/2}}^{0}\sigma(z)\mathrm{d}z, \quad (24.21)$$

in which the density anomaly in layer k is given with sufficient accuracy by (see [25])

$$\sigma_k = \frac{\rho_k-\rho_0}{\rho_0} = 0.68\times 10^{-5}T_k^2.$$

Therefore,

$$\int_{z_{k+1/2}}^{0}\sigma(z)\mathrm{d}z = 0.68\times 10^{-5}\left(\sum_{j=1}^{k}T_j^2 h_j\right). \quad (24.22)$$

In Eqs. (24.18)–(24.20) the transition conditions at the interfaces between two layers are thought to be incorporated. For instance, $(T_{xz}, T_{yz})_{1/2}$ are the wind shear stresses $(t_x^{\mathrm{wind}}, t_y^{\mathrm{wind}})$ in the x- and y-directions, and for $w_{1/2}$ in Eq. (24.18), $\partial\zeta/\partial t$ is substituted, which is the linearized version of (24.11). Similarly, $(T_{xz}, T_{yz})_{N+1/2}$ are the basal shear stresses for which the sliding law (24.15), (24.16) are substituted, and in the shallowness assumption $w_{N+1/2}=0$ since $\boldsymbol{v}\cdot\boldsymbol{n}=0$ at the basal surface.

The transition conditions at interior layer interfaces for the stress components T_{xz}, T_{yz} are parameterized as

$$T_{xz}|_{k+1/2} = \rho_0\nu_{v|_{k+1/2}}\frac{u_{k+1}-u_k}{\frac{1}{2}\left(h_{k+1}^x+h_k^x\right)},$$
$$T_{yz}|_{k+1/2} = \rho_0\nu_{v|_{k+1/2}}\frac{u_{k+1}-u_k}{\frac{1}{2}\left(h_{k+1}^y+h_k^y\right)}, \quad (24.23)$$

in which the superscripts x and y indicate that for h a value of the finite difference approximation of the h-values of Eqs. (24.9) is to be substituted, see footnote 4 in Chap. 23.

Analogously, the vertical component of the heat flux vector at the kth interior interface ($k\geqslant 1$) is givenby

$$Q_z|_{k+1/2} = (\rho_0 c_p \kappa_v)_{k+1/2} \frac{T_{k+1} - T_k}{\frac{1}{2}(h_{k+1} + h_k)}. \tag{24.24}$$

At the free surface one either prescribes the air temperature (= surface water temperature) or the atmospheric heat input,

$$T_1 = T^{\text{atm}} \quad \text{or} \quad Q_z|_{1/2} = Q^{\text{atm}}, \tag{24.25}$$

whereas at the basal surface the temperature is prescribed

$$T = T_{\text{base}}. \tag{24.26}$$

The replacement of the original three-dimensional Eqs. (24.8), (24.10) by the layer-depth averaged Eqs. (24.18)–(24.20) has led to a new system of spatially two-dimensional coupled partial differential equations. Boundary conditions in the system must be fulfilled at the bounding (vertical side) walls of each layer. The common statements are the requirement of impermeability (no flow through the wall) and/or the prescription of the temperature in the ground at that depth. Of course, other options are equally possible, see [25].

The layered equations governing the baroclinic motion are differential equations for the velocity and temperature fields within the lake; they contain phenomenological coefficients, namely

- the horizontal (A_0) and vertical (ν_v) momentum exchange coefficients,
- the horizontal (κ_h) and vertical (κ_v) thermal diffusion coefficients,
- the drag coefficient (c_w) of the wind shear stress and
- the drag coefficient (c_b) of the basal friction law (24.16).

Experimentally determined values for A_0 and κ_h are of the order of 1 m^2s^{-1}, those in the vertical direction depend considerably upon the stratification, whereby values within the metalimnion are much smaller than those in the epi- and hypolimnion. Diffusion of momentum and energy is therefore blocked at the thermocline. The drag coefficient c_b at the basal surface will be assigned the value $c_b = 0.002$ [27].

The wind drag coefficient c_w, to be used for evaluation of the wind shear stresses (24.13) was parameterized according to

$$c_w = \begin{cases} 1.5 \times 10^{-3}, & W < 5.2\,\text{ms}^{-1}, \\ 1.5 + 1.5 \times 10^{-3} \sin\left(\frac{\pi}{2} \frac{W - 1.5}{10.1}\right), & 5.2 \leqslant W \leqslant 15.1\,\text{ms}^{-1}, \\ 3.0 \times 10^{-3}, & W > 15.1\,\text{ms}^{-1}, \end{cases} \tag{24.27}$$

and is dimensionless in this form. This formula, however, was not calibrated with data from Lake Zurich, but it was calibrated by a fit of Lake Ontario data, originally due to SCHWAB (1981) [20]. It also has been successfully used for Lake Superior by SYDOR and OMAN [26].

We emphasize that in finite difference integration schemes of differential equations of the transport-type [Eqs. (24.18)–(24.20)] numerical instabilities and false wave

propagation may arise. These can and must be avoided by adding artificial numerical diffusion. The amount of this additional numerical diffusion depends, among other things, chiefly upon the number of layers, N, and the grid size, Δs, of the finite difference representation. It decreases both with an increase of N and a decrease of the grid size Δs.

Now, the necessary numerical diffusion that maintains the computational stability is so large that its diffusivities surpass their physical counterparts. As a consequence, experimental values for κ_h and κ_v need not be known, since their values are overshadowed by the numerical diffusion. Depending upon the discretization one has $A_0 \in [1, 10]\ \mathrm{m^2 s^{-1}}$ (the physical value is about $1\ \mathrm{m^2 s^{-1}}$); moreover, for the vertical momentum diffusivity the formula

$$\nu_v = \frac{\mathfrak{F}\left(\nu_0, \frac{1}{\rho_0}\nu_1 \|\boldsymbol{t}^{\mathrm{wind}}\|\right)}{\left(1 + \frac{10}{3} Ri\right)^{1/2}}, \quad Ri \equiv \frac{\frac{g}{\rho}\frac{\partial \rho}{\partial z}}{\left(\frac{\partial \boldsymbol{v}_H}{\partial z}\right)^2} \tag{24.28}$$

has proved to be adequate. Ri is the RICHARDSON number, $\boldsymbol{t}^{\mathrm{wind}}$ the wind shear traction at the free surface, and ν_0 and ν_1 are coefficients such that

$$\nu_0 \in [0, 0.0025]\,\mathrm{m^2 s^{-1}} \qquad \nu_1 \in [25, 100]\,\mathrm{s}$$

with specific values depending upon discretization. Formula (24.28) has been used by SIMONS [24] and BENNETT [1] with $\mathfrak{F}(x, y) = x + y$. OMAN [19] also tested the case $\mathfrak{F}(x, y) = \mathrm{Max}(x, y)$. Formula (24.28) accounts for the fact that (i) ν_v grows with the strength of the wind, (ii) that even for $\|\boldsymbol{t}^{\mathrm{wind}}\| = 0$ the diffusivity ν_v does not vanish and (iii) that ν_v decreases with increasing RICHARDSON number. Clearly, since Ri assumes its maximum in the thermocline, ν_v assumes there its minimum. It is also clear that the false numerical diffusion can contribute to the distortions of the numerical solutions of the integrated equations, of which the size can be so large that the numerical model may reproduce the physical processes rather unrealistically. Such situations must be avoided. By reduction of the finite difference net size and increase of the number of layers, this can often be achieved.

Finally, mention must be made that, owing to rapid pulsations which are often observed in the computed horizontal velocity components, BENNETT [1] proposed to replace in (24.19) the horizontal momentum diffusion terms

$$A_0 \Delta_H (h_k u_k) \quad \text{and} \quad A_0 \Delta_H (h_k v_k) \tag{24.29}$$

by

$$A_1 \frac{\partial}{\partial x} (\mathrm{div}_H (h \boldsymbol{v}_H)_k) \quad \text{and} \quad A_1 \frac{\partial}{\partial y} (\mathrm{div}_H (h \boldsymbol{v}_H)_k)\,. \tag{24.30}$$

This replacement improved the numerical performance by reducing the unphysical pulsations in the horizontal and vertical velocities. BENNETT also selected the diffusivity A_1 as $A_1 = \frac{1}{4}\Delta x \Delta y f$, where $\Delta x \Delta y$ is the area of the horizontal grid and f is the CORIOLIS parameter. We shall return to this in the next section.

24.4 An Almanac of Tests

24.4.1 Selection of the Standard Test Conditions

The validity and accuracy of the numerical model has been tested by conducting a great number of computations under a standard wind scenario but varied parameters which are characteristic for the physics of Lake Zurich on the one hand and the discretization of its geometry and the construction of the layered equations on the other hand. The Lake Zurich measurements of the 1978 field campaign have amply indicated that the water velocities and temperature are subject to relatively conspicuous appearances of oscillations with approximate periods of 45, 24–25 h, and 18 h; these results are based on a stratification due to the temperature profile displayed in Fig. 24.5.[4]

Because these oscillations constitute a sizeable imprint of the observations for durations of several days, it is only natural to request that the model is capable of reproducing oscillations of current and temperature with these periodicities. Obser-

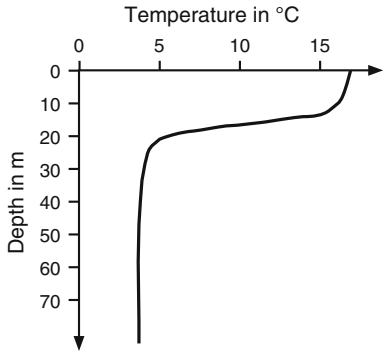


Fig. 24.5 Temperature distribution which was used as initial temperature profile for the test runs and the evaluation of the first three fundamental seiche periods, 44, 24–25 and 18 h

[4] Seiches in enclosed lakes or ocean basins are eigensolutions of the barotropic or baroclinic water wave equations. The eigenvalues are expressed as the seiche periods and eigenfunctions as the modes of the vertical thermocline displacements associated to the eigenvalues. For many situations it is sufficient to express the stratification by a two-layer system, a light epilimnion and a dense hypolimnion, whose interface mimics the thermocline. For Lake Zurich the internal (baroclinic) seiche has been analyzed by HORN et al . [4] for the stratification of Lake Zurich during the field campaign of 1978. The eigenperiods of the fundamental and first two higher order modes of the two-layered Lake Zurich have been determined as approximately 45, 25 and 18 h, respectively. For an extensive treatment of seiches, see [12].

vations in a number of Alpine lakes (Lake Constance, Lake Geneva, Lake of Lugano, Lake Zug, Lake Zurich, …) have in fact indicated that post-storm lake dynamics during summer stratification, more often than not, trigger some modes of the internal seiches, which accompany the circulating motion due to direct wind forcing and persist after wind cessation. The following conditions were used as standard set-up for all test computations:

- At $t < 0$ the lake is assumed at rest (no motion) and subject to a stable stratification with a temperature profile as shown in Fig. 24.5.
- At $t = 0$ a wind from *west* sets suddenly in, uniform in space, HEAVISIDE in time and of strength $7.5\,\mathrm{m\,s^{-1}}$. This is a rather strong wind for Lake Zurich, but occurring generally more than once during summer months. Its duration is taken to last 24 h (1 day) when it stops abruptly. The computations are continued after wind cessation for a total of 96 h (4 days).
- Because the artificial numerical diffusion of the finite difference approximation overshadows the size of the physical diffusion of the temperature, only numerical diffusion is taken into account.

Table 24.1 lists the conditions for which computations have been performed. The 15 tests comprise a summary of many and are discussed below with focus on a comparison of computed results with observations, deduced from the field campaign in August-September 1978. The intention is, to reproduce the variations of the current and temperature distributions in the aftermath of a strong Föhn storm on 12–14 September 1978 and lasting (in its strong phase) approximately 24 h. The water motion reacted with a growing circulation flow which was accompanied by an additional internal surge, which initiated an internal seiche of approximately 44 h period lasting for several days. According to Tables 24.1 and 24.2 the number and distribution of layers, time step and grid size were varied as were various parameterizations of the diffusivity of momentum in the vertical, (24.28), and in the horizontal, (24.29), (24.30), directions. We give here only an epitome of the more detailed presentation [19].

24.4.2 Inferences From Tests 1 to 4

All tests conditions are collected in Tables 24.1 and 24.2. The analysis began with an 8 layer model of 5 m thickness each in the top 7 layers and a net of spatial grids of 500 m side length. With the numerical diffusivities as stated for test Runs 1 & 2, computations were performed with time steps of 10 and 5 min to see that the results (selected isotherm-depth-time series, horizontal layer velocity distributions at various time slices and time series for vertical velocities, generally at 15 m depth) were not much altered with the finer resolution. So, subsequent computations were all performed with a 10 min time step.

Consider now Fig. 24.6. Because the region between the 8- and 12 °C-isotherms corresponds to the metalimnion, and since the motion of the isotherms accurately mimics the vertical displacement of the water particles, Fig. 24.6 provides reliable

Table 24.1 List of the 15 test runs performed in [19]

Run Nr.	Number of layers	Timestep [min]	Grid size [m]	$\mathfrak{F}\left(\nu_0, \frac{1}{\rho_0}\nu_1\|\boldsymbol{t}^{\text{wind}}\|\right) = \mathfrak{F}(x, y)$	ν_0 [m^2s^{-1}]	ν_1 [s]	A_0 [m^2s^{-1}]	A_1 [m^2s^{-1}]
1	8	10	500	y	0	100	10	–
2	8	5	500	y	0	100	10	–
3	10	10	500	y	0	100	10	–
4	13	10	500	y	0	100	10	–
5	8	10	500	y	0	100	1	–
6	8	10	500	y	0	100	–	$\frac{1}{4}\Delta x\Delta y f$
7	8	5	250	y	0	100	–	$\frac{1}{4}\Delta x\Delta y f$
8	18	10	500	$x + y$	0.0025	25	–	$\frac{1}{4}\Delta x\Delta y f$
9	18	10	500	y	0	100	–	$\frac{1}{4}\Delta x\Delta y f$
10	18	10	500	y	0	25	–	$\frac{1}{4}\Delta x\Delta y f$
11	18	10	500	$Max(x, y)$	0.0004	25	–	$\frac{1}{4}\Delta x\Delta y f$
12*	18	10	500	$Max(x, y)$	0.0004	25	–	$\frac{1}{4}\Delta x\Delta y f$
13×	18	10	500	$Max(x, y)$	0.0004	25	–	$\frac{1}{4}\Delta x\Delta y f$
14†	18	10	500	$Max(x, y)$	0.0004	25	–	$\frac{1}{4}\Delta x\Delta y f$
15‡	18	10	500	$Max(x, y)$	0.0004	25	–	$\frac{1}{4}\Delta x\Delta y f$

The vertical diffusivity ν_v is given by (24.28) and A_1 arises in (24.29)
∗ $f = 0$ in the momentum equations
× No advection in the momentum equations
† Maximum epilimnion temperature reduced to 16 °C
‡ Maximum epilimnion temperature reduced to 14 °C

information about the *computed* vertical motion within the metalimnion. This is shown in Fig. 24.6 for models with 8, 10 and 13 layers (see Table 24.2 for interface depths and layer thicknesses). Under the action of wind stress from *west*, the equilibrium water is pushed towards east, and that in the hypolimnion towards west. This generates a set-up with downwelling in the eastern part of the lake and upwelling in the deep part of the lake near Zurich. This can be observed in the graphs of Fig. 24.6 during slightly more than 24 h. Only about half a day after wind cessation the isotherm motion is reversed as downwelling at station 4 and upwelling at station 10. No oscillatory motion can be observed. The corresponding isotherm-depth-time series of the 10 and 13 layer model computations are very similar to those of the 8 layer model. No essential differences are visible except those which can be traced back to the differences of the initial temperature distribution. The panels of Fig. 24.6 show that a computational forecast of internal waves by increasing the number of layers alone cannot be achieved. However, the induced motion of the water masses in the 10 and 13 layer runs are very similar to the results for Run 1 (8 layers). In this sense the layer model is considered consistent, but it is not sufficiently accurate.

Table 24.2 Depths of interfaces (Roman) and layer thicknesses (italic) in meters for runs with 8, 10, 13 and 18 layers

8		10		13		18		Temp. Run 18 in °C
0		0		0		0		
	5		*5*		*4*		*4*	19
5		5		4		4		
	5		*5*		*2*		*2*	19
10		8		6		6		
	5		*5*		*2*		*2*	18
15		11		8		8		
	5		*5*		*2*		*2*	17
20		14		10		10		
	5		*5*		*2*		*2*	15
25		17		12		12		
	5		*5*		*2*		*1*	14
30		20		14		13		
	5		*5*		*2*		*1*	12
35		25		16		14		
	105		*10*		*2*		*1*	10
140		35		18		15		
			20		*2*		*1*	9
		55		20		16		
			85		*5*		*2*	8
		140		25		18		
					10		*2*	7
				35		20		
					20		*2*	7
				55		22		
					85		*2*	6.5
				140		24		
							4	6
						28		
							7	5
						35		
							20	4
						55		
							30	4
						85		
							55	4
						140		

← Interface depths ← Layer thickness

The last column lists the initial temperatures in °C of the layers for the 18 layer model

The attenuation of the on-setting oscillation before the second oscillation period was formed could also be observed in other computational results of the three different layer models, e.g., the vertical and horizontal velocities within a particular layer at the measuring stations (Fig. 24.1) and the temperature and horizontal velocity

distributions in the various layers at time slices 1, 2, 3, 4 days. Figure 24.7 shows the vertical velocities at 15 m depth (approximately the thermocline depth) at the stations 4, 6, 11, 12 for Run 1 (8 layers). In coincidence with the graphs of the isotherm-depth-time series one sees during the first day of wind action an upward velocity in the deep western lake part (stations 4 and 6) but in the shallow eastern lake part (stations 11 and 12) a downward velocity. After wind cessation these velocities change; they turn into a downwelling in the western part of the basin and an upwelling in the eastern part. These motions, however, die out almost entirely after the second day.

Even though the response of the lake to the prescribed wind load is qualitatively correctly reproduced during direct wind action—the isotherms rise in the western part of the lake (stations 4 and 6) and fall in the eastern part (stations 11 and 12)—one expects after wind cessation after one day a somewhat faster and stronger reaction of the isotherms than shown in Figs. 24.6 and 24.7. In particular, the isotherm displacements (rising in the western and falling in the eastern part of the lake) from equilibrium levels should have led to an eigenoscillation with a period of approximately 45 h. Instead, a relatively fast decay ensues into the rest position without any sign of oscillation.

The attenuation of the motion must be related to the annihilation of energy. Internal waves are created by an exchange of kinetic and potential energy. For an analytical two-layer model HEAPS and RAMSBOTTOM in 1966 [2] proved that annihilation of energy by friction at the lake bottom can impede internal waves. Destruction of potential energy can have the same effect. Now, the numerical diffusion, which is necessary for computational stability, destroys the potential energy, whilst the too large (but equally needed) horizontal momentum exchange (A_0) destroys the kinetic energy. A better understanding of the 'failure' of the model in this respect can be obtained from the time series of the energies, which are shown for Run 1 and Run 4 (8 and 13 layers) in Fig. 24.8.[5]

[5] Here, the energies of the total water masses are meant. The potential and kinetic energies are defined as follows:

$$
\begin{aligned}
PE &= \int\int\left(\int_{-H}^{\zeta}\rho(z)gz\,\mathrm{d}z\right)\mathrm{d}x\mathrm{d}y\\
&= \int\int\left(\int_{-H}^{\zeta}\left[\rho_0+(\rho-\rho_0)\right]z\mathrm{d}z\right)\mathrm{d}x\mathrm{d}y\\
&= \sum_{ij}\left[\left(\zeta^2-H^2\right)\rho_0 g+\rho_0\sum_k\left(z_{k-1/2}^2-z_{k+1/2}^2\right)\sigma_k\right],\\
KE &= \int\int\left(\int_{-H}^{\zeta}\rho(u^2+v^2)\mathrm{d}z\right)\mathrm{d}x\mathrm{d}y\\
&= \sum_{ij}\left[\sum_k\rho_0\left(h_k u_k^2+h_k v_k^2\right)\right],\\
E &= PE+KE.
\end{aligned}
$$

The double integral has to be performed over the surface of the lake.

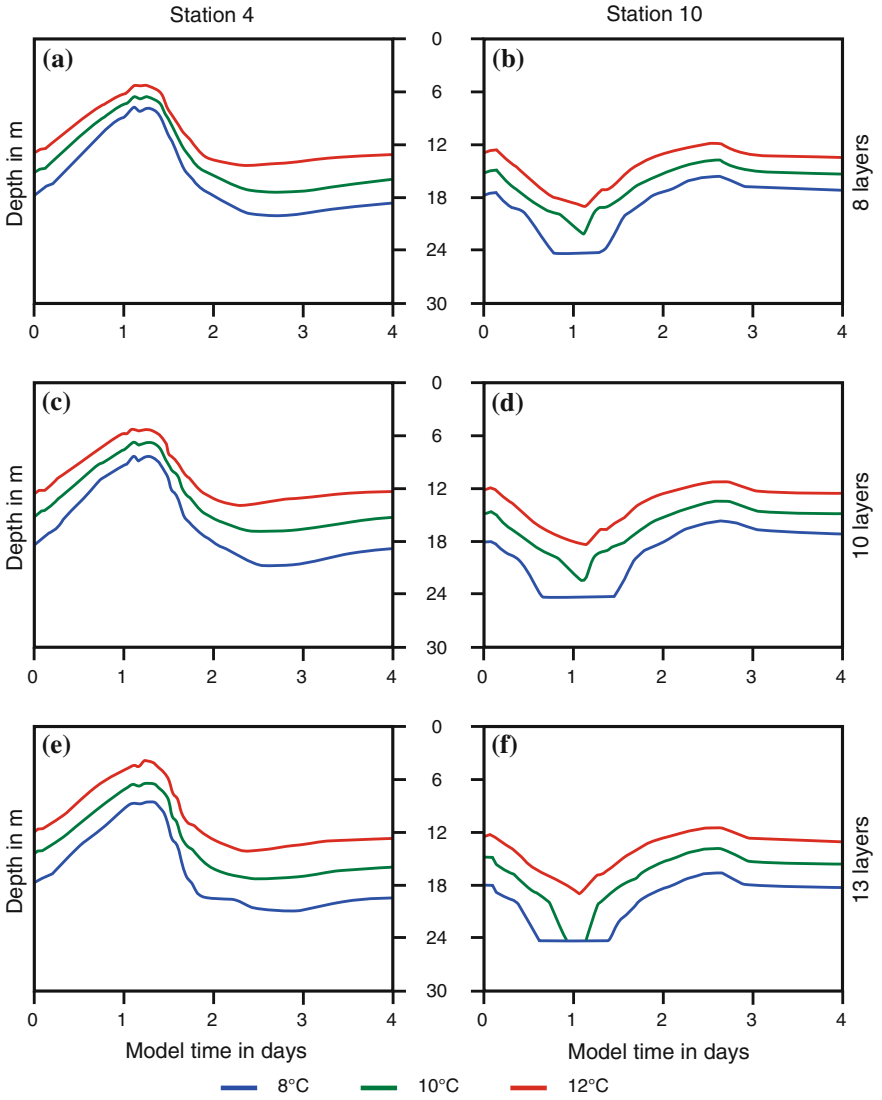


Fig. 24.6 Time series of the isotherm depths for the 8-, 10- and 12 °C-isotherms in stations 4 (*left panels*) and 10 (*right panels*), see Fig. 24.1, as functions of time (during 4 days). Results are computed for an 8 layer (*top row*), 10 layer (*middle row*) and 13 layer (*bottom row*) model. Modeling conditions are given in Tables 24.1 and 24.2. The wind load was impulsively applied at $t = 0$, blowing from west, uniform in space and HEAVISIDE in time and with strength of 7.5 ms^{-1}, and lasting for 24 h after which it suddenly stopped. The horizontal line in the panels of station 10 identifies the lake depth at that station, from [19] © Versuchsanstalt für Wasserbau, Hydrologie und Glaziologie an der ETH Zürich, reproduced with permission

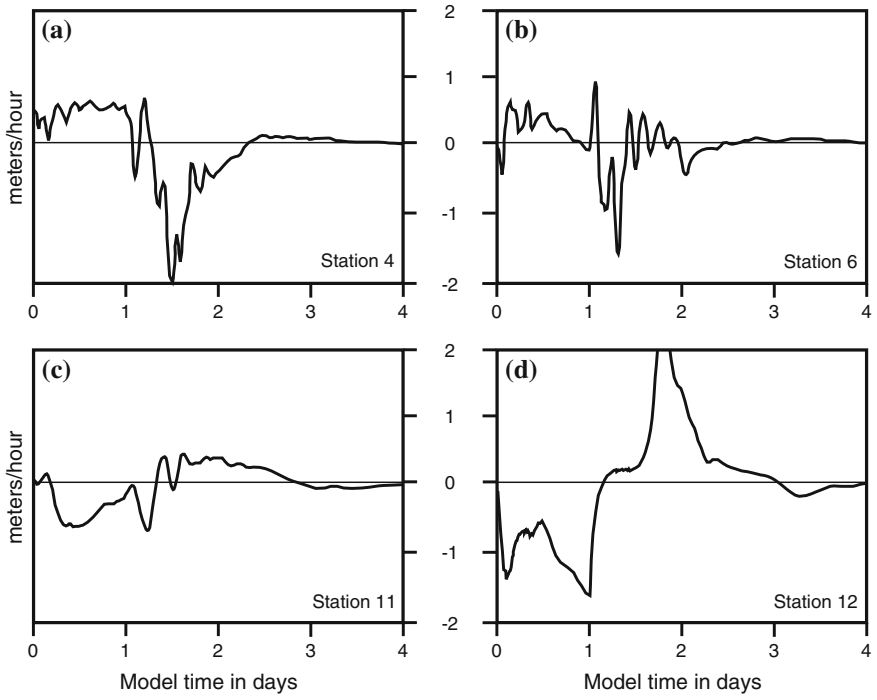


Fig. 24.7 Vertical velocities in 15 m depth (upper interface of the fourth layer), computed for Run 1, corresponding approximately to the thermocline depth at the stations 4, 6, 11, 12 for the same wind as in Fig. 24.5, from [19] © Versuchsanstalt für Wasserbau, Hydrologie und Glaziologie an der ETH Zürich, reproduced with permission

In the plots one expects a slow attenuation of the total energy $E = PE + KE$ after one day, whereby the kinetic and potential energies oscillate rhythmically in an out-of-phase fashion and with a period of 22.5 h (corresponding to half the period of the fundamental seiche mode). However, this is not seen in the two graphs of Fig. 24.8, where the energy dies out far too quickly. After one day the decay of the potential energy is by far larger than the gain of potential energy. In this process the destruction of the potential energy by numerical diffusion and the destruction of the kinetic energy by excessive horizontal exchange of momentum play a decisive role. The numerical diffusion is an inescapable fact of the finite difference approximation and cannot be removed. But the size of this numerical diffusion has been reduced in Runs 3 and 4 by better vertical resolution with an increase of the number of layers. However, essentially *hardly any sizeable improvement of the results was achieved*. As the only other possibility we have at our disposal the reduction of the size of the horizontal momentum exchange.

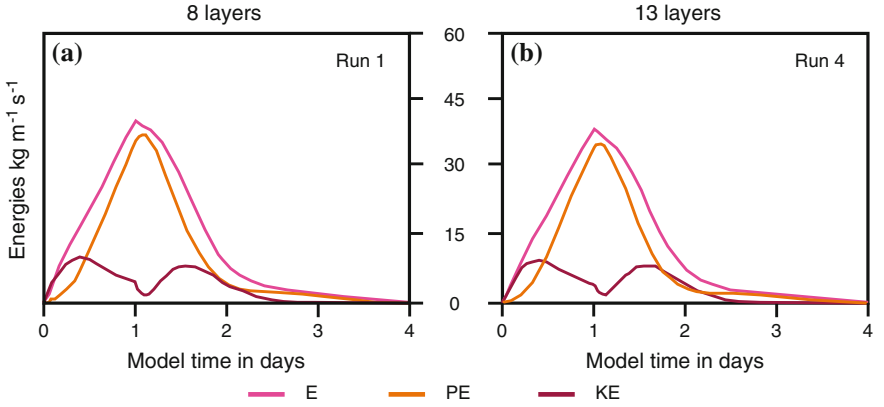


Fig. 24.8 Time series of the total energy, E, the potential energy, PE and the kinetic energy (KE) for Run 1 (8 layers) and Run 4 (13 layers). One would expect a rhythmic alteration between kinetic and potential energy paired with a slow attenuation of the total energy with time, from [19] © Versuchsanstalt für Wasserbau, Hydrologie und Glaziologie an der ETH Zürich, reproduced with permission

24.4.3 The Role of the Horizontal Momentum Exchange

In Run 5 the exchange coefficient of horizontal momentum was reduced to the more realistic value of $A_0 = 1\,\mathrm{m^2 s^{-1}}$; all other initial conditions were left unchanged as for Run 1. Figure 24.9 (top panels) shows the 8-, 10- and 12 °C-isotherm-depth-time series for an impulsively applied wind from west of 7.5 $\mathrm{m^{-1}}$ strength as before. In comparison to the results displayed in Fig. 24.6 conspicuous differences are discerned. The isotherms at station 4 (and more generally in the deep western part of the lake, not shown here) rise during the first day to higher levels. Correspondingly, the isotherms at station 10 (and generally in the entire eastern part of the lake, not shown here) fall to deeper depths than in Run 1. At the end of the second day the return of the isotherm depths to higher levels is somewhat faster. However, subsequent expected oscillations do not occur; the isotherms return on days 3 and 4 slowly and without any sign of oscillation to their rest positions. The short periodic pulsations after wind cessation at station 4 (and 6 and 9, not shown here) are not seen at stations (10, 11 and 12, not demonstrated here); so, the deep lake part reacts more sensitively than the shallow part. The likely reason for this behavior is an increased instability of the numerical scheme, in which the vertical diffusivity in Run 1 is set to zero after wind cessation [see (24.28) with $\mathfrak{F}(x, y) = y$ for Run 1]. This lack of numerical momentum exchange leads to instabilities of the vertical velocity components in the deep lake part, but not in the shallow basin. Figure 24.10 (top panels) gives corroboration for this: As soon as the wind stops, conspicuous short periodic pulsations set-in.

OMAN [19] also demonstrates that the reduced value of the horizontal momentum exchange affects the horizontal velocities at the measuring stations which are up

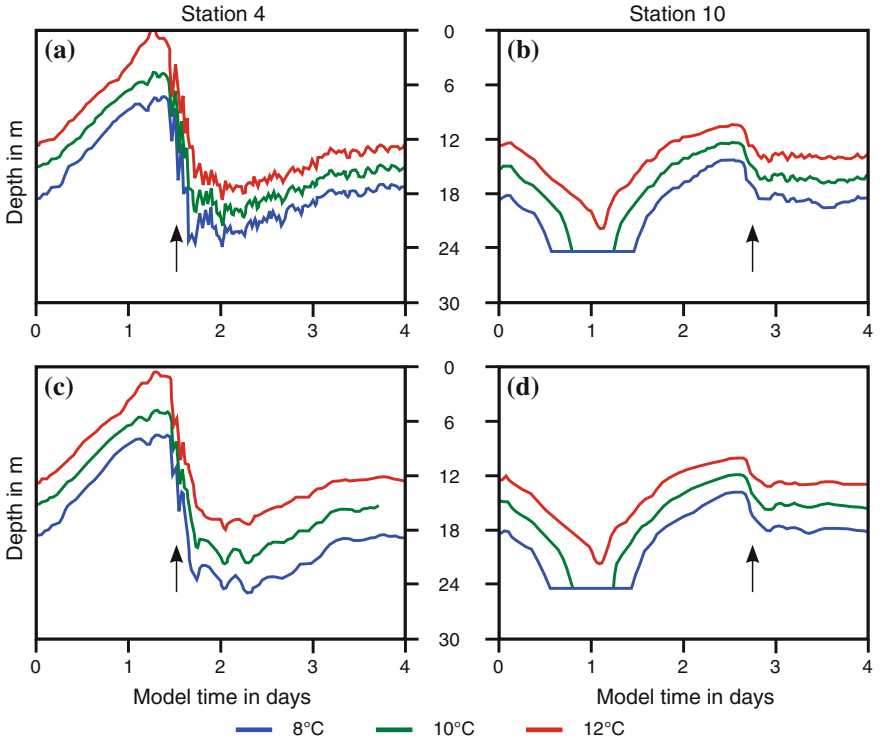


Fig. 24.9 Time series of the isotherm depths for the 8-, 10- and 12 °C-isotherms in stations 4 (*left panels*) and 10 (*right panels*) (see Fig. 24.1) as functions of time during 4 days. Results are computed for an 8 layer model. Modeling conditions are given in Tables 24.1 and 24.2 as Runs 5 and 6. The wind load was impulsively applied at $t = 0$, blowing from west, uniform in space and HEAVISIDE in time and with strength of 7.5 m s^{-1}, and lasting for 24 h, after which the wind suddenly stopped. Panels in the *top* display the results for the horizontal exchange according to (24.29), those in the *bottom row* are based on (24.30) instead. *Arrows* show the internal surge, from [19]. © Versuchsanstalt für Wasserbau, Hydrologie und Glaziologie an der ETH Zürich, reproduced with permission

to 50 % larger when $A_0 = 1$ m^{2}s^{-1} than when $A_0 = 10$ m^{2}s^{-1}. Moreover, after wind cessation, the velocity vector plots in the 8 layers after 2, 3, 4 days show some orientation indeterminacies of the horizontal velocities which are more conspicuous in the deep than in the shallow basin part and are, therefore, evidently related to the instabilities of the isotherm-depth-time series and the vertical velocities.

To avoid these numerical difficulties requires some kind of smoothing, either in the horizontal plane or in the vertical direction. Because the vertical momentum exchange exerts a much greater influence on the horizontal velocities than the horizontal momentum exchange [23], a horizontal smoothing will now be introduced. If this is done, the annihilation of kinetic energy that goes with it, must be kept as small as possible; however, the smoothing operation should also dampen the pulsations in the vertical velocity components as far as possible, to avoid the destruction

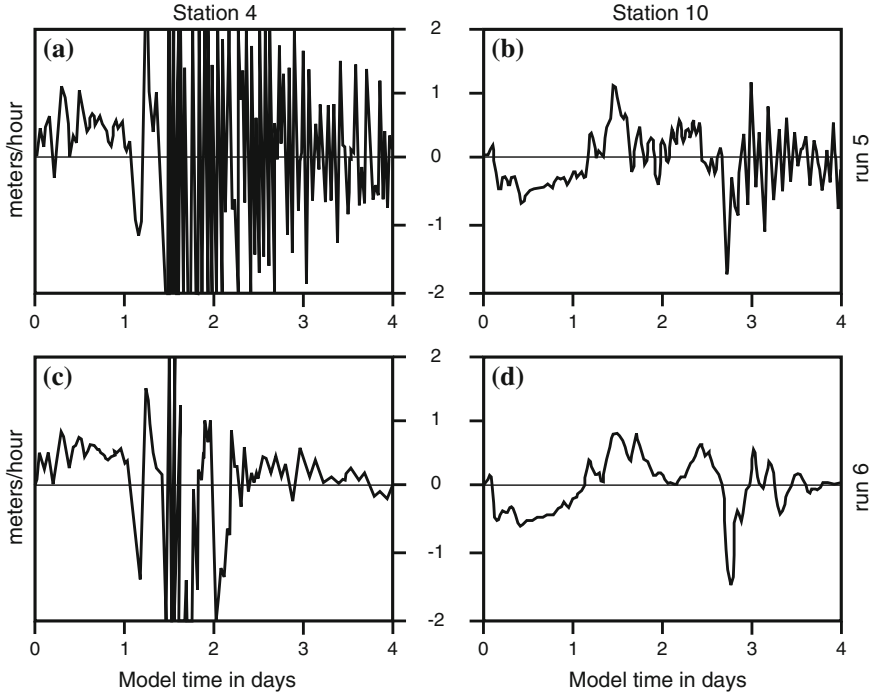


Fig. 24.10 Time series of the vertical velocities at the upper interface of the fourth layer in Runs 5 and 6. As soon as the explicit vertical momentum exchange vanishes, large short periodic pulsations occur in the time series of the vertical velocity components. *Top panels* for Run 5 with the classical momentum exchange $\mathfrak{F}(x, y) = y$, see (24.28), and the horizontal momentum exchange (24.29), *bottom panels* for the horizontal momentum exchange due to BENNETT, (24.30), from [19]. © Versuchsanstalt für Wasserbau, Hydrologie und Glaziologie an der ETH Zürich, reproduced with permission

of the potential energy. One possibility to achieve this is to introduce a smoothing which is proportional to the straining of the horizontal velocity field. The horizontal areal straining in layer k of thickness h_k is given by $(\mathrm{div}_H(h\boldsymbol{v}_H))_k$ and its x- and y-derivatives have the same dimension as $\Delta_H(h_k u_k)$; therefore, BENNETT [1] proposed the replacement of the horizontal exchange terms (24.29) by (24.30), where A_1 is a coefficient with the same physical dimension as A_0. Its size likely depends on the area of the surface element $\Delta x \Delta y$ of the horizontal grid and is proportional to it. $A_1 = a\Delta x \Delta y\, f$ has the correct physical dimension $[\mathrm{m}^2\mathrm{s}^{-1}]$ if a is dimensionless. BENNETT and OMAN and chose $A_1 = \frac{1}{4}\Delta x \Delta y\, f$.[6]

In Run 6 the horizontal diffusive momentum exchange was parameterized in this way according to formula (24.30); else conditions of Run 1 were implemented. The lower panels of Figs. 24.9 and 24.10 show the isotherm-depth-time series and ver-

[6] On the f-plane, f is constant, on the β-plane, f is formed as the arithmetic mean of the four edge points of the grid element.

tical velocities for this run at stations 4 and 6 as described in the figure captions. The short periodic pulsations of the isotherms, which were observed in Run 1 after wind cessation, are no longer observed with comparable intensity at station 4. Furthermore, as one can see from Fig. 24.10 in the lower left panel, the pulsation of the vertical velocity components are equally much reduced; they are, however, not completely removed. At the other stations of the deep basin part there are still times, after wind cessation at which exaggeratedly large pulsations of the vertical velocity components are not removed (see [19], large pulsations of the vertical velocities not demonstrated here). These pulsations are regularly observed after a rapid downwelling of the isotherms. Such a rapid sinking of the light water masses must necessarily be accompanied by corresponding activation of buoyancy forces, a fact which induces the overly large pulsations of the vertical velocities, which hardly can be suppressed.

A sudden downwelling of the isotherms after cessation of the stormy wind from west has been observed in Lake Zurich and can be connected with the passage of an internal temperature front, which is comparable to a meteorological front [16]. Such internal fronts manifest themselves always by a sudden lowering of the isotherms, which propagate from one end of the lake to the other end. Figure 24.11[7] shows

[7] MORTIMER, in the unpublished report [16] describes this figure as follows: 'On an expanded time scale covering four days of record, 11–14 Sept., the depth fluctuations of the 10 and 8 °C isotherms are plotted over a 14 m (8–22 m) depth range for stations 4, 6 (supplemented by nearby station 5), 9, 10, 11, i.e. for a series arranged along the length of the basin. Also plotted are the u (i.e. EW) and v (NS) components of wind speed squared (a measure of stress) at station 6. Because the depth ranges within which temperatures were measured (by a chain of thermistors) varied from station to station, some of the isotherms [in the figure] are discontinuous. For example, the station 6 isotherms on Sept.12 exited (upwards) out of and re-entered (downwards) into the diagram at the 12 m level (the top of the range for station 6). Part of the missing information is supplemented by the 9 to 12 m record from nearby station 5. During Sept. 12, a day of large depth fluctuations following the storm, the station 10 and 11 isotherms exited (downwards) and re-entered (upwards) at 19 and 18 m, the respective lower limits of the ranges at those stations. Also, the upper edge [of the figure], at 8 m, is the upper limit for station 4, above which the isotherm depth was not recorded. In each case the points of exit and re-entry are indicated by horizontal arrowheads. The station 9 isotherms, on the other hand, always remained within the confines of the figure.

[Close examination of the figure] discloses the following sequence. Before the strong wind impulse started on 11 September, the weather had remained relatively calm since September 9th. During the morning of the 11th the isotherms at 4 and 6 were falling, while those at 9, 10 and 11 were rising, following the pattern of a preexisting internal first-mode seiche (44 h period) … That pattern was evidently destroyed by the wind impulse, which started at about 14:00 h later. By that time (22:00 h) the isotherm-depth trends had reversed, with 9, 10 and 11 falling rapidly and with 4 and 6 rising rapidly (near A) around midnight. The behavior (a strongly developing tilt of the thermocline, upward in the NW and downward in the SE portion of the basin) is clearly consistent with the strong east going component of the wind.

The wind's strength fell somewhat just after midnight, but rose to a second maximum around 05:00 to 07:00 h. Sept. 12th, falling thereafter to much lower levels at about 14:00 h on that day. The ensuing calm spell lasted for several days thereafter. As soon as the wind stress was removed, the tilted thermocline began to swing back until (at about midnight 12/13 Sept.) the isotherms at all stations were again near the pre-storm mean levels. The swing continued during the early morning of Sept. 13th with upward isotherm motion at 9, 10 and 11 and downward motion at 4 and 6, initiating the damped internal seiche oscillation […]. Although the first mode (44 h) component was dominant,

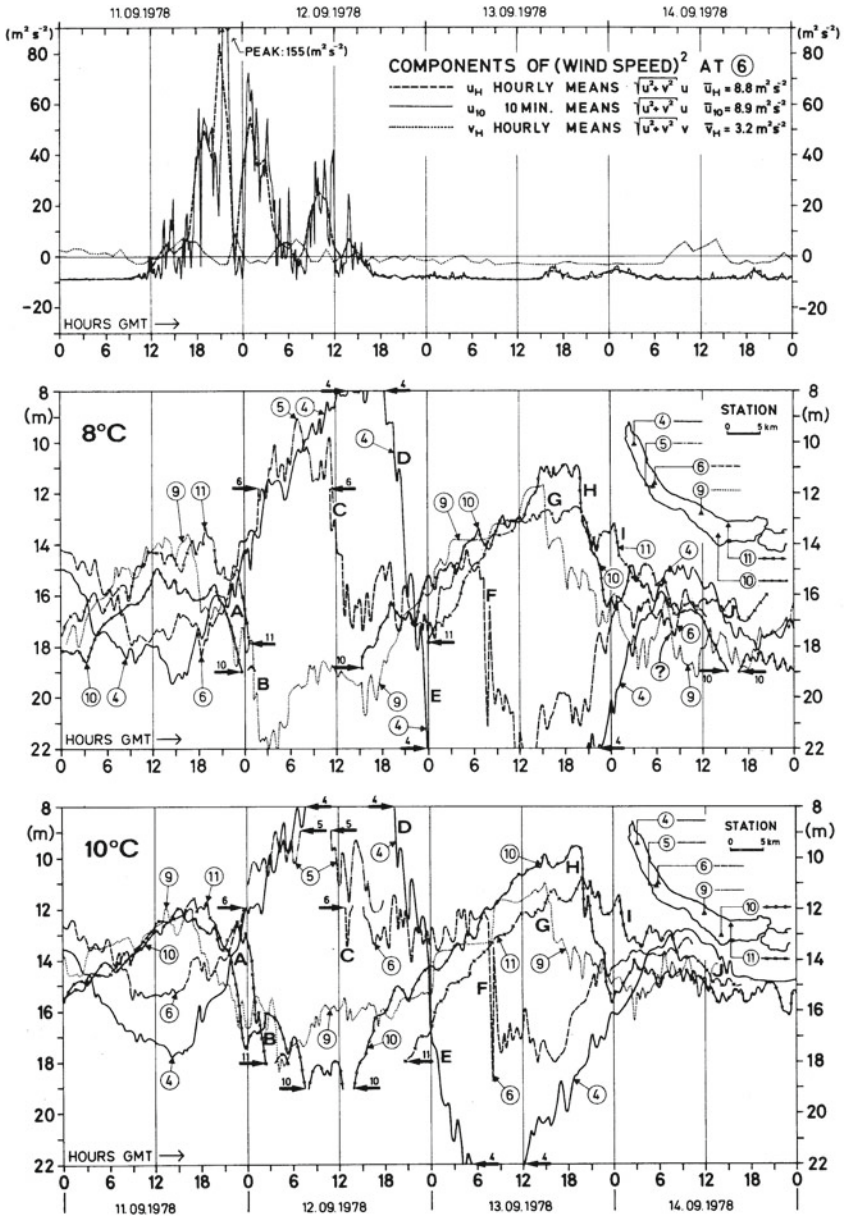


Fig. 24.11 Time series of the 8- and 10 °C-isotherms at stations 4, 6, 9, 10 from 11 to 14 September 1978. [Parts of measurements of station 5 are also shown to extend the upper cut-off of the measurements at station 6.] Station numbers are shown *encircled*. *Horizontal arrows* indicate when an isotherm depth leaves or re-enters the measuring regime. The letters *A* to *J* indicate when the internal front passes by the indicated station. In the *top panel* the *u*- (towards west) and *v*-components (towards east) of the squared velocity of station 6, 3 meters above the water surface are displayed, from [16]. © Versuchsanstalt für Wasserbau, Hydrologie und Glaziologie an der ETH Zürich, reproduced with permission

the time series of the measured 8- and 10 °C-isotherms after a strong wind from west between 11 and 14 September 1978. As in the model, the wind approaching from west lasted approximately one day and stopped almost abruptly afterwards. The hourly mean wind-shear stress was, however, smaller than in the model. For this reason, only a qualitative comparison of the measured and computed isotherm depths is meaningful. The measured isotherms of station 4 reach their top level shortly after wind cessation and fall quickly afterwards, compare Fig. 24.11. The small pulsations of the isotherms, which are shown in the model at station 4 can also be seen in the measured isotherms. The down-fall of the isotherms at station 6 and the corresponding rise at station 9 occur also soon after wind cessation. Temperature fronts can be recognized in the computed as well as measured time series; these occur at times at which isotherms suddenly fall. At first, this is seen at station 4 at the deep north-western end of the lake. A sudden fall of the isotherms occurs later at station 6 and even somewhat later at stations 9 and 10. From the distances between the stations and the times, at which the front passes these stations, the speed of the front can be computed. This speed is 0.7 $\mathrm{km\,h^{-1}}$ in the model and 1.1 $\mathrm{km\,h^{-1}}$ in nature.

The influence of the internal surge, in Fig. 24.9 indicated by the arrows, can also be seen in vector plots of the horizontal velocities in the different layers. When this surge, which started its motion at the north-western lake end (station 4) progresses along the lake axis towards south-east, it leaves behind a (computed) horizontal velocity field, which is not stably ordered, whereas the corresponding horizontal velocities in front of the surge are robust in their orientation. This fact is corroborated by figures, displaying the horizontal velocity distributions after two and three days, see [19].

As already remarked, the front of the computed isotherms moves too slowly. In frequency space the model must be regarded as inaccurate. On the other hand, size and form of the computed displacements of the isotherms out of their rest position are essentially correct. In particular, the isotherm depths demonstrate inclinations across the lake which rotate counter-clockwise around the lake with near shore velocity of approximately 0.35 $\mathrm{m\,s^{-1}}$, [16]. This behavior, which is visible in the isotherm plots, is attributable to the effect of the CORIOLIS force and interpretable as the fundamental KELVIN wave of a two-layer model. The spatial distribution of the isotherms after wind cessation can therefore be regarded as reliable, however, the time at which this distribution exists, occurs too late and the attenuation is too large as in earlier runs. The computed internal seiche dies out too quickly.

The influence of the internal surge, indicated as arrows in Fig. 24.9, is also recognizable in the horizontal velocity distribution at the end of the second day as displayed in Fig. 24.12, in which the horizontal velocity distribution is displayed in the 8 layers

---

that oscillation was evidently far from simple […]. A further complication is the presence of internal surges. Compared with many lakes, in which the first modal oscillation generated by such a storm would persist for many cycles, the Zurich oscillation appears to be relatively strongly damped. Perhaps this may be a consequence of the shallow topography at the southeastern end of the basin, forming a shelf upon which more of the internal wave energy is absorbed than is reflected. This is in contrast to the steeper topography at the northwestern end, at which a greater portion of the energy is reflected,' from [16].

for Run 6. It can be seen that the horizontal velocities in the shallow south-eastern part of the lake are well ordered in their orientations; the velocities correspond here to the expected return currents. In the deep north-western part of the lake, i.e. behind the temperature front, however, the velocity field is distorted and not well constrained in the orientation. Once the temperature surge has passed the entire lake, this orientation fuzziness has reached the entire horizontal velocity field. This has been demonstrated in [19] by showing the analogous figure for the end of the third day.

The spatial distribution of the 8 °C-isotherm surface from 1 day 0 h to 2 days 8 h, in steps of 4 h, is displayed in Fig. 24.13. As evident from Fig. 24.12 after 2 days the water of the epilimnion flows from Rapperswil towards Zurich and that in the hypolimnion in the opposite direction. During this period the CORIOLIS force causes a deviation of the water motion to the right, transverse to the actual velocity vector; in other words, the warm water of the epilimnion drifts towards the right shore (e.g. Meilen, see Fig. 24.1), whilst the hypolimnion water of the epilimnion drifts towards the left shore (e,g, Horgen). Because of the corresponding shift of epilimnetic and hypolimnetic water masses, the isotherm depths along the right shore must fall relative to their equilibrium positions; and along the left shore they must rise instead. In other words, the isotherms are inclined across the lake. Figure 24.13, which displays snapshots of the 8 °C-isotherm surface every 4 h from 1 day 0 h and 2 days 8 h (after wind set-up) this transverse inclination is clearly seen. The isotherms at Meilen are about 10 m deeper than at Horgen, however, only as long as the epilimnetic water flows after wind cessation from east towards Zurich.

For the far too rapid attenuation of the oscillation after wind cessation a false transformation of the potential and kinetic energy and vice versa is responsible. In Fig. 24.14 time series of the total energy (E), the potential energy (PE) and the kinetic energy (KE) are displayed for Run 5 (left panel, reduced horizontal momentum exchange $A_0 = 1\ \mathrm{m^2 s^{-1}}$) and for Run 6 (right panel, BENNETT's areal viscosity). Compared to the corresponding plots for Runs 1 and 4, shown in Fig. 24.8 the recovery of kinetic energy after wind cessation is improved, however, still too much potential energy is destroyed. Incidentally, notice that in Run 5 at the end of the second day the potential energy increases again. This growth is fairly monotonous and possibly attributable to the excessively large pulsations of the vertical velocities. This potential energy is no longer transformed into kinetic energy. Moreover, because of the horizontal smoothing of the velocity field, kinetic energy is persistently destroyed; this does not occur in Run 6 with BENNETT's viscosity where the kinetic energy is larger. However, further oscillations after day 2 do neither occur in this run.

24.4.4 Influence of the Horizontal Grid Size

All previous computations were performed with horizontal square grids of 500 m side length; this led frequently only to three grid points across the width of Lake Zurich. Run 7 was performed with 250 m side length; the remaining conditions were the same as in Run 6 except that the time increment is now 5 min (in order to fulfill

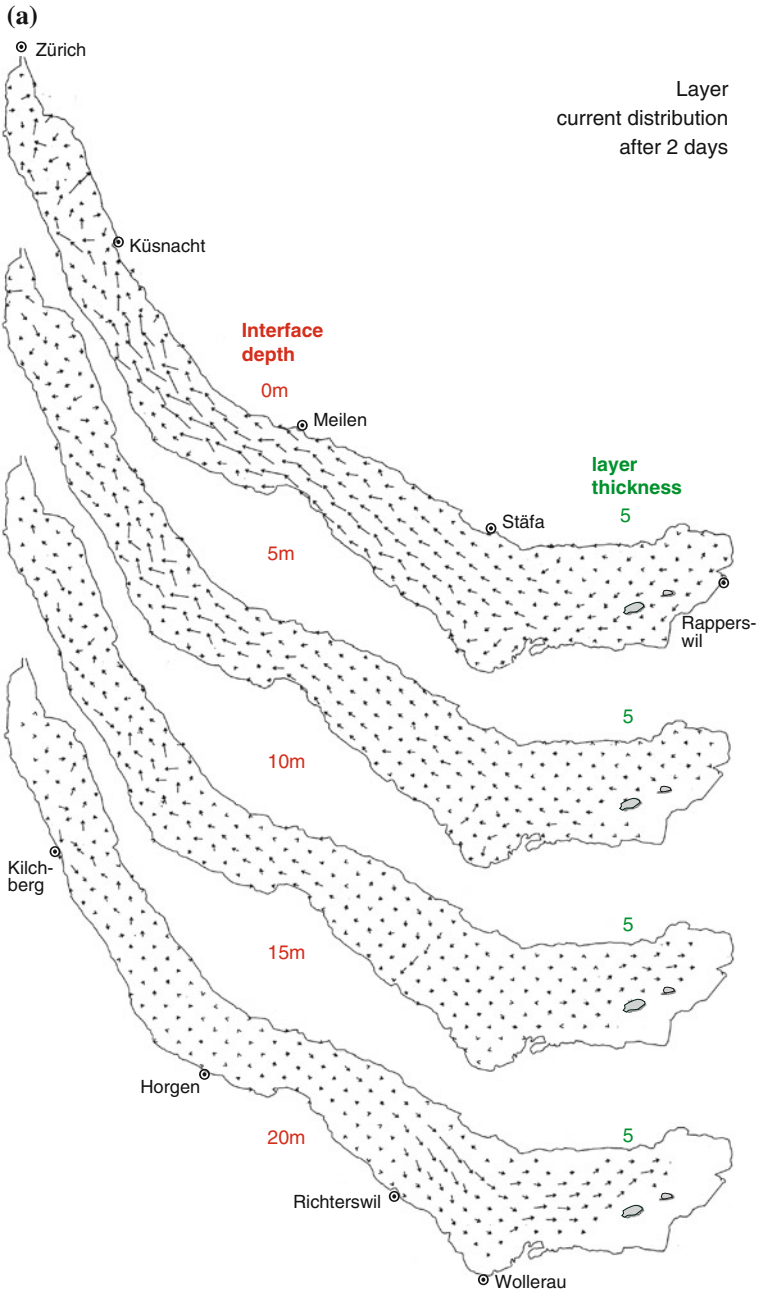


Fig. 24.12 Distribution of the horizontal velocity in layers 1 to 8 after 2 days. *Arrows* with the length of the grid size correspond to 15 cm s^{-1} in layers 1–5 and 3 cm s^{-1} in layers 6–8, from [19]. © Versuchsanstalt für Wasserbau, Hydrologie und Glaziologie an der ETH Zürich, reproduced with permission

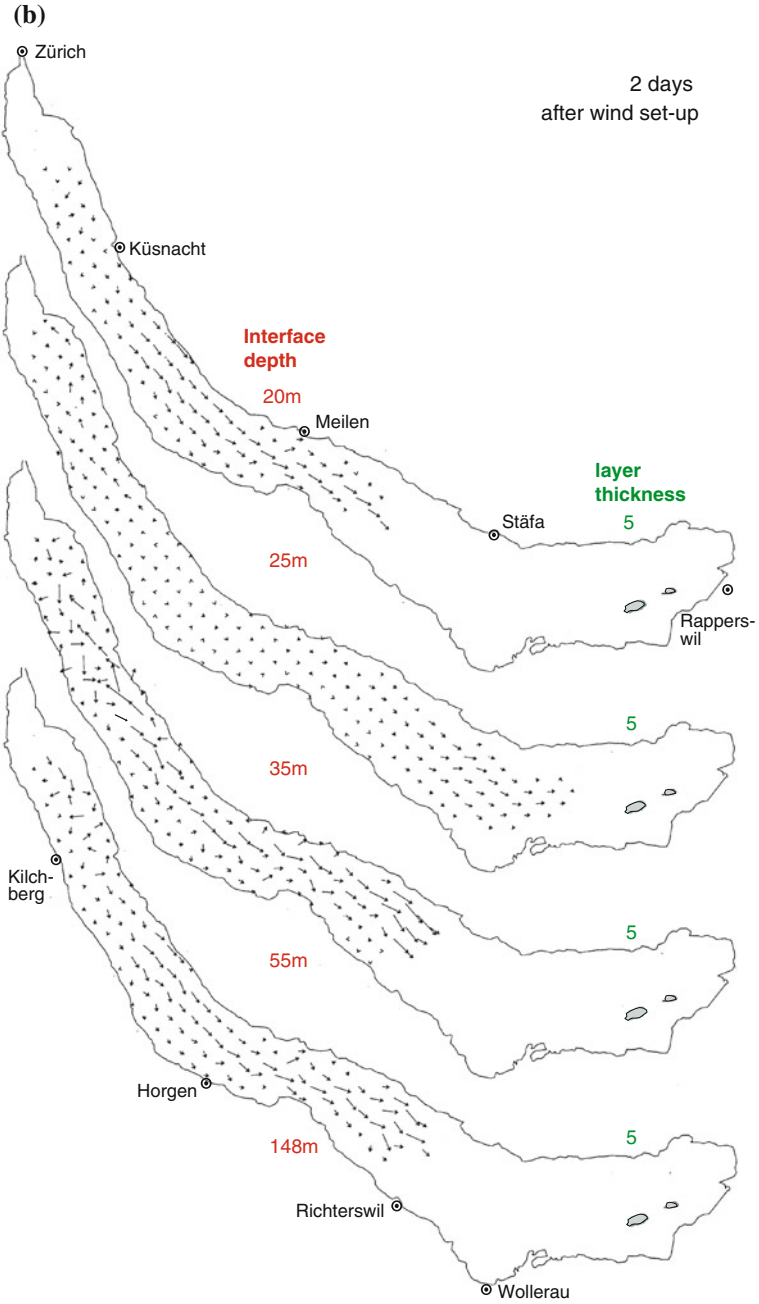


Fig. 24.12 (continued)

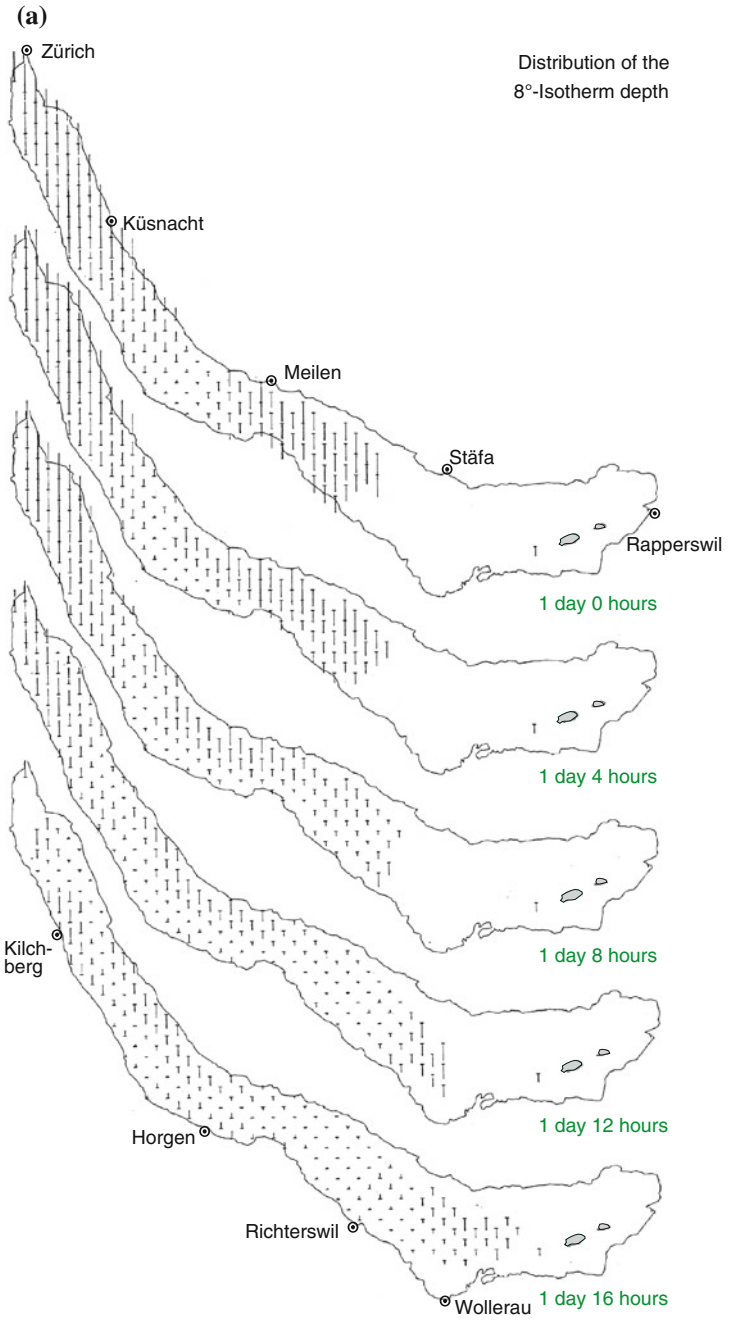

(a)
Zürich
Distribution of the
8°-Isotherm depth
Küsnacht
Meilen
Stäfa
Rapperswil
1 day 0 hours
1 day 4 hours
1 day 8 hours
Kilch-
berg
1 day 12 hours
Horgen
Richterswil
Wollerau
1 day 16 hours

Fig. 24.13

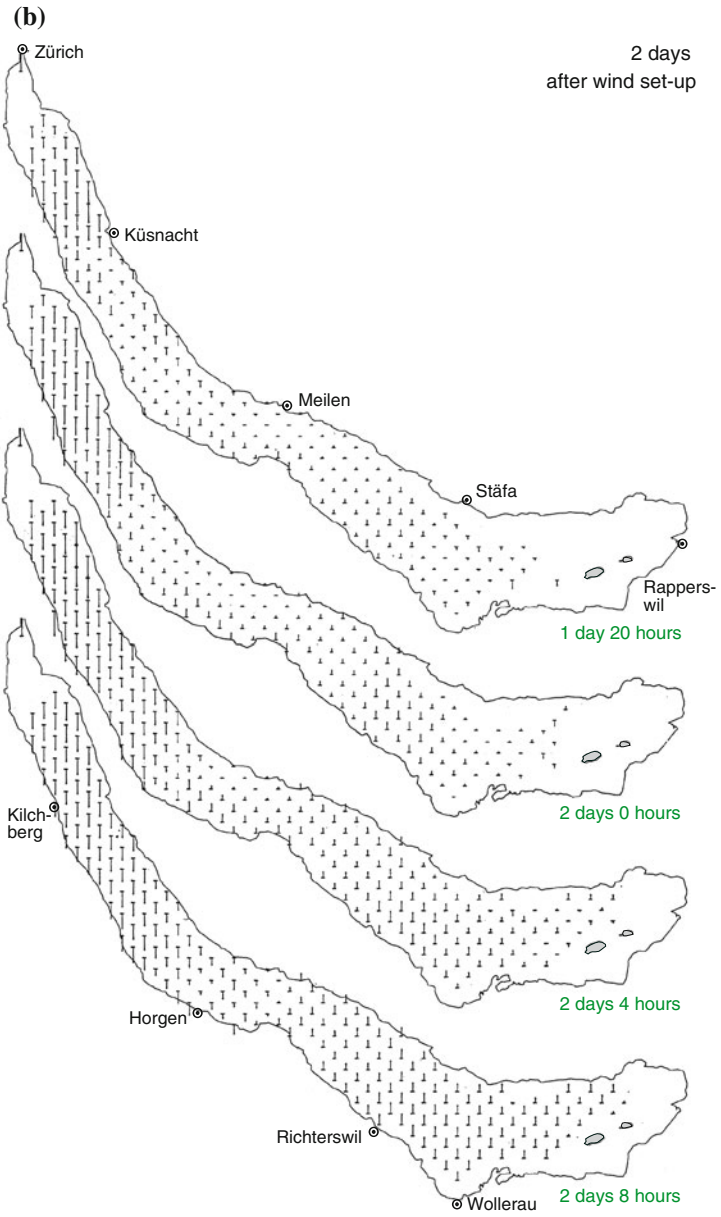


Fig. 24.13 (continued) Distribution of the 8 °C-isotherm depths every 4 h after wind cessation from 1 day 0 h to 2 days 8 h, computed with BENNETT's areal viscosity. The symbols ⊥ and *top* indicate mean positive (*upwards*) and negative (*downwards*) deviation of the isotherm depth from the equilibrium depth. The vertical bar of the length of the grid size corresponds to 6 m, from [19]. © Versuchsanstalt für Wasserbau, Hydrologie und Glaziologie an der ETH Zürich, reproduced with permission

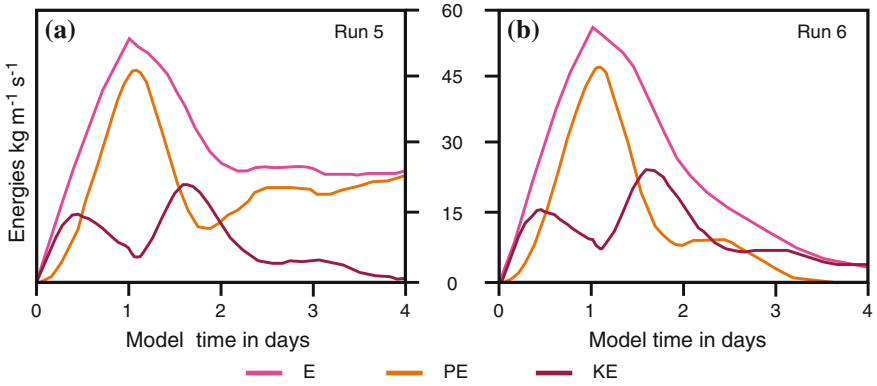


Fig. 24.14 Time series of the total energy (E), the potential energy (PE) and the kinetic energy (KE) for Runs 5 and 6. One expects with time a rhythmic attenuation between kinetic and potential energies paired with a slow decay of the total energy, from [19]. © Versuchsanstalt für Wasserbau, Hydrologie und Glaziologie an der ETH Zürich, reproduced with permission

the CFL condition); moreover, BENNETT's areal viscosity was used. These changes increased the computational time by a factor of 8.

Figure 24.15 displays the isotherm depths and the vertical velocity in 15 m depth at stations 4 (representative for the deep part of Lake Zurich) and 6 (representative for the shallow part of Lake Zurich). Results look very similar to those of Run 6 (see Figs. 24.9 and 24.10). However, the unrealistically large pulsations of the vertical velocities (panels (c), (d) in Fig. 24.15) are somewhat suppressed, since the horizontal exchange coefficient is now four times smaller. The time slice, when these pulsations arise, coincides with the passage of the surge and manifests itself as oscillations around a mean value of the isotherm depths. Except for this numerical noise the isotherm depth-time series are hardly different from those of Run 6. In particular, the speed of the internal down-stroke surge moving towards south-east did not change and is still too slow. After the passage of this front the isotherms return slowly to their rest position without a sign of a continued 44 h oscillation. This can also be seen in the plots of the energies which are nearly identical to those of Run 6 and not shown here.

24.4.5 Influence of the Vertical Momentum Exchange

None of the further attempts to find better performance of the model and obtained with other vertical diffusivities different from (24.28) was successful; so, additional trial tests to reduce the turbulent diffusion were conducted with an additional increase of the number of layers to 18 (see Table 24.2). The selection of the layer thicknesses was such that four 1 m thin layers cover the metalimnion. The temperatures of the upper most layers are also larger than for Runs 1 to 7 and closer to the temperatures of the 1978-experiment; this leads also to a faster response of the model. With the

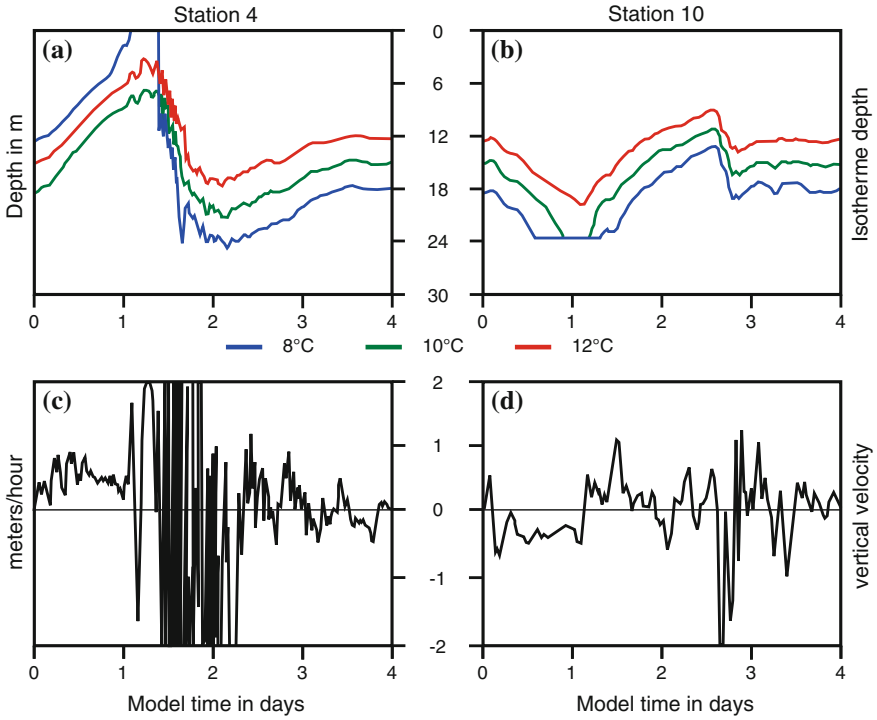


Fig. 24.15 Isotherm-depth-time series for the 8-, 10- and 12 °C isotherms at stations 4 and 10 (*panels* **a**, **b**). Time series of the vertical velocity components in 15 m depth (*panels* **c**, **d**). BENNETT's exchange coefficient is used and a grid net of 250 m side length. Note, the pulsations at station 4 (deep part of the lake), which are missing at station 10 (shallow lake part), from [19] © Versuchsanstalt für Wasserbau, Hydrologie und Glaziologie an der ETH Zürich, reproduced with permission

distribution of the layers according to the choice of Table 24.2 a reduction of the numerical diffusion is expected. Runs 8 to 11 are performed with this 18-layer model and the temperature distribution of Table 24.2 and a vertical diffusivity shown in (24.28), and with $\mathfrak{F}(x, y)$ as listed in Table 24.1, and $x = \nu_0$, $y = \frac{1}{\rho_0}\nu_1 \mid \boldsymbol{t}^{\text{wind}} \mid$. As this table shows, Runs 9 and 10 were performed with $\nu_{=}0$, so implying vanishing diffusivity after wind cessation and thus expected large turbulent pulsations in the isotherm depth and vertical velocity time series at and after the passage of the down-stroke surge in the deep basin, but no such evidence in the shallow basin. Furthermore, because ν_1 is four times larger in Run 9 than in Run 10, this should lead to a higher rise of the isotherms during wind and faster response of the model, i.e., a steeper down-stroke of the surge in Run 10 than in Run 9. The disadvantage of relatively strong pulsations is counter-balanced in Runs 8 and 11 by choosing $\nu_0 \neq 0$ and selecting $\mathfrak{F}(x, y) = x + y$ (Run 8) and $\mathfrak{F}(x, y) = \text{Max}(x, y)$ (Run 11). Of these two, Run 11 has been decided to be the better, even though the turbulent pulsations are somewhat larger, since the speed of the internal surge is 0.9 km h^{-1} and thus closest

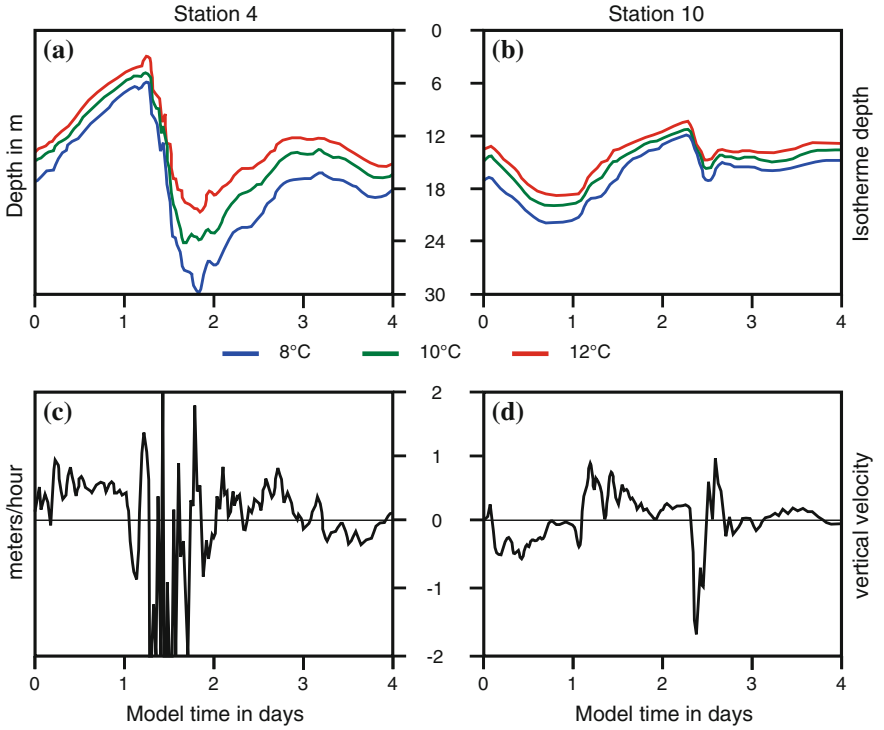


Fig. 24.16 Time series of the isotherm depths (*top panels* **a**, **b**) and the vertical velocities (*bottom panels* **c**, **d**) at stations 4 and 10 for the 18 layer model, computed with BENNETT's areal viscosity and a vertical viscosity according to (24.28) with $\mathfrak{F}(x, y) = \mathrm{Max}(x, y)$, from [19]. © Versuchsanstalt für Wasserbau, Hydrologie und Glaziologie an der ETH Zürich, reproduced with permission

to the measured speed of 1.1 km h^{-1}. Most of the above described results is educated guessing based on knowledge gained from earlier results, but it is all documented in [19] as solid numerical findings. Figure 24.16 collects the results of Run 11 for the isotherm depth time series and vertical velocities at stations 4 and 10.

Corroboration that with Runs 8 to 11 a stepwise improvement of the seiche response of Lake Zurich can be achieved, can particularly well be given by the time series of the energy plots of Fig. 24.17, which also shows the employed vertical diffusivity formulae. As evident, the coefficient ν_1 is responsible for a larger or smaller value of the potential energy during wind action. The larger the maximum value is (after about 1 day), the larger will also be the vertical velocities and displacements of the isotherm depths. Figure 24.17 discloses in the order of Runs 9, 8, 10, 11 a stepwise better and better transformation of the potential energy into kinetic energy and vice versa. Oscillations of these energy forms are discernible over all four days, and the time series of the potential and kinetic energies are approximately in counter-phase. Even though the differences of the oscillation features between the individual runs are not very conspicuous, Run 11 can be regarded as the best.

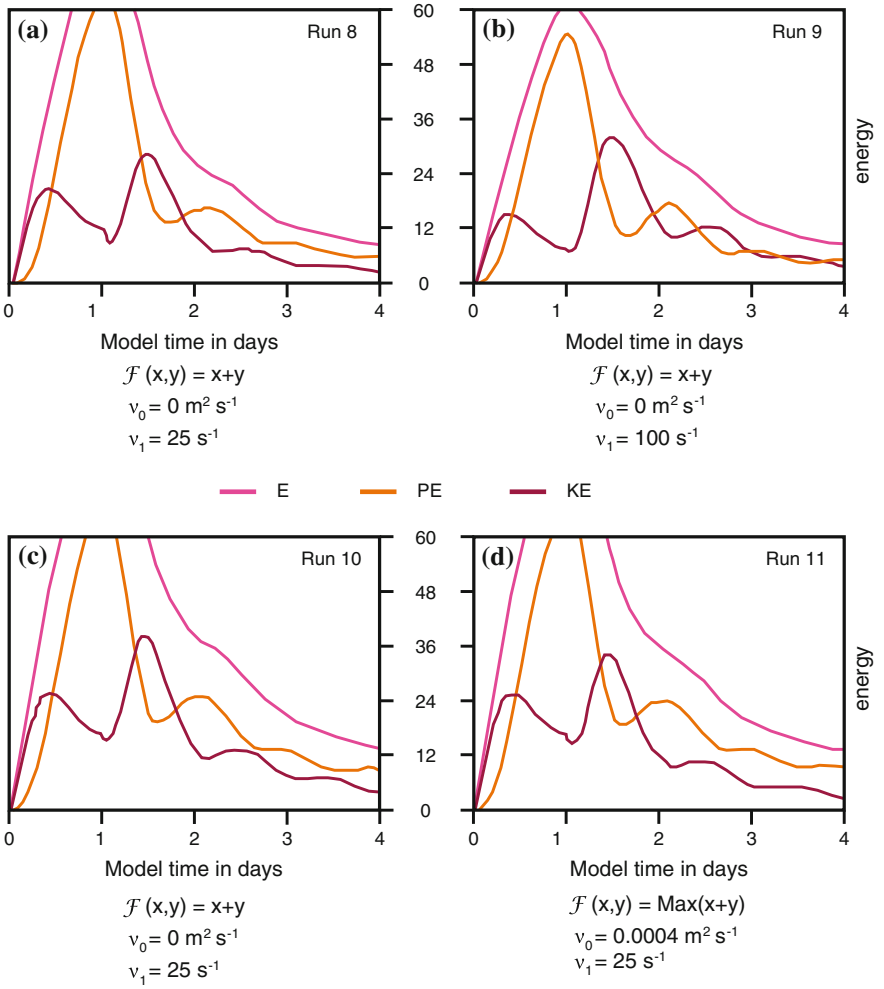


Fig. 24.17 Time series of the total energy (E), potential energy (PE) and kinetic energy (KE) for Runs 8, 9, 10, 11. The formulae give information, in which form the vertical momentum diffusivity (24.28) was used for the respective run. The 18-layer model with BENNETT's areal viscosity was used according to Tables 24.1 and 24.2, from [19]. © Versuchsanstalt für Wasserbau, Hydrologie und Glaziologie an der ETH Zürich, reproduced with permission

If the exchange of vertical momentum during the active wind phase is small, then the more kinetic and potential energies can develop, a fact which leads to larger velocities and greater displacements of the isotherms. However, a smaller value for the coefficients of vertical momentum exchange also leads to a larger distortion of the velocity field, which is caused by the false pulsations of the vertical velocities. This distortion seems to perturb the transformation of the kinetic into the potential

energy. For instance the increase of the kinetic energy after wind cessation in Run 10 is smaller in Run 9 at the same time (and for which the vertical momentum exchange during the active wind phase is smaller than in Run 10), even though the potential energy in Run 10 is larger than in Run 9. This also explains, why the oscillations in both runs appear as more conspicuous in Run 9 than in Run 10. Comparison of Runs 9 and 10 in Fig. 24.17 also leads us to conclude that for non-vanishing vertical momentum exchange after wind cessation the kinetic energy drops faster than otherwise. Moreover, a small value of the exchange coefficient, which should be maintained for stability reasons, affects the internal seiche response only marginally, quite opposite to Run 8, for which the internal seiche response is hampered because of a too large value of the exchange coefficient.

24.4.6 Effects of Coriolis Force, Momentum Advection and Stratification

Effect of CORIOLIS forces. It is often argued that for dynamical processes the ROSSBY radius of deformation is a measure for estimating whether effects of the CORIOLIS force need to be accounted for or can be neglected. It is then claimed that for lakes whose extent (width) L is small in comparison to the (internal) ROSSBY radius of deformation,

$$L \ll R \equiv \frac{c}{f}, \qquad c \equiv \sqrt{g \frac{\Delta \rho}{\rho} \frac{h_1 h_2}{h_1 + h_2}},$$

CORIOLIS forces can be dropped from the momentum equations. In the above formula, c is the phase speed of a wave and its value on the right-hand side is for a two-layer model with top layer thickness h_1 and bottom layer thickness h_2 and corresponding densities ρ_1 and ρ_2, $\Delta \rho = \rho_2 - \rho_1 > 0$. This is a valid approximation for the evaluation of the phase speed of KELVIN waves but not the identification of their counter clockwise rotation on the northern Hemisphere. POINCARÉ-type wave dynamics and topographic ROSSBY waves cannot be explained by dropping the CORIOLIS forces from the momentum equations, and neither can they be dropped in wind induced circulation dynamics since variable topography activates gyration effects due to the CORIOLIS forces. MORTIMER [16] has shown that measured isotherm-depth-time series during and after the 11–14 September 1978 storm indicate KELVIN wave effects, i.e., counter-clockwise motion of a selected isotherm 'hump' around Lake Zurich. At mid-lake positions 5 and 7, see Fig. 24.1, 8 °C-isotherm maxima occur during a fundamental seiche period of 44 h in counter phase and this demonstrates a transverse inclination of the isotherm depth, oscillating between station 5 and 7 with this period. This was corroborated by computations of Run 12 by performing computations with and without CORIOLIS force [19]. This transverse inclination was weak, but clearly discernible (approximately, differences in isotherm depth maxima

of 1 m). In computations with $f = 0$ this difference was not seen, compare also Figs. 24.12 and 24.13.

Effect of horizontal momentum advection. In early oceanographic circulation models horizontal advection in the momentum equations is often ignored simply because these terms are non-linear and therefore hardly accessible to analytical handling for the construction of analytical solutions even in simple wind forcing scenarios to basins of simple geometry. This was the major reason for dropping these terms. Computations in Run 13 in which the advective terms are dropped, revealed qualitatively that the isotherm-depth and vertical velocity time series are similar to those of Run 11. The difference of the results with and without these terms, however, is sufficiently significant that dropping these terms is not recommended. True, the computational efforts are somewhat larger, but today's computers can easily cope with these effects.

Effects of stratification. It is well known that during a period of relatively calm and sunny weather the temperature profile in the epilimnion reaches rather high values close to the free surface as shown in Fig. 24.18 as the solid blue line. During a storm even of relatively short duration the wind shear stress introduces high turbulent activity, which mixes the epilimnion water, which then leads to a temperature profile as shown in Fig. 24.18 in black and green lines. The black step-approximation shows the temperature representation of the 18-layer model and the red and green versions show the approximations used for Runs 14 and 15.

The time series of the computed isotherm depths at stations 4 and 10 for Runs 14 and 15 are shown in Fig. 24.19. As long as the wind lasts, the time series are very similar to those of earlier runs (with 19 °C epilimnion temperature). Generally, the colder the epilimnion is, the larger are the isotherm displacements. Furthermore, the internal seiche propagates slower and the amplitudes of the isotherm oscillations are smaller and the seiche periods longer.

In summary, it may be concluded that of all tested variants the 18-layer model with BENNETT's areal viscosity and the viscosity function $\mathfrak{F} = \mathrm{Max}(x, y)$ seems to be the best suited version. With this model the currents which are exposed to direct wind forcing can realistically be quantified; however, the motion which follows after wind cessation is too dissipative. The post-storm continuing current distribution can hardly realistically be reproduced, let alone be predicted. In spite of this, the model remains meaningful insofar as it correctly predicts the water motion, which is directly exposed to the wind. Improvements are to be sought in the use of non-hydrostatic models, higher resolutions of the finite difference discretization and higher order turbulence closure.

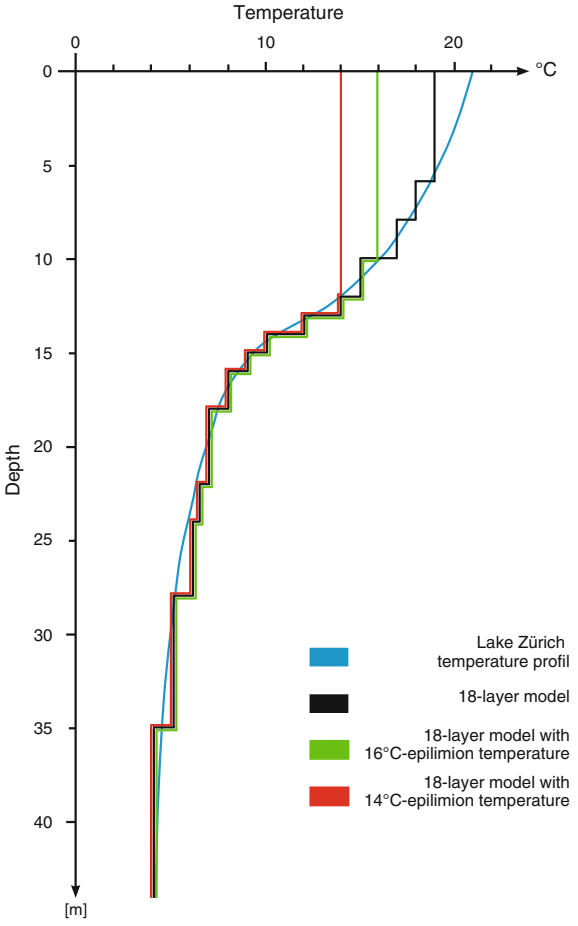


Fig. 24.18 Lake Zurich mean temperature profile (*solid smooth curve, blue*) during the Aug-Sept. 1978 field campaign used for the 18 layer model (*black solid step-wise approximation*) and for Run 14 (*red version*) and Run 15 (*green version*) with reduced epilimnion temperatures of 16 and 14 °C, respectively

24.5 Comparison of Model Output with Field Observations of 1978 Lake Zurich Campaign

The reliability of the model has been tested by numerical simulations of current and temperature distributions due to the stormy wind from west, which was blowing from 11 to 12 September 1978. The reaction of the lake during and after this wind event has been described in detail by MORTIMER [16] and in a brief epitome in connection with Fig. 24.11. Because this wind was blowing in near counter phase with the already existing seiche in the lake, it caused a relatively abrupt return of the motion of the isotherms. The consequences of this constellation manifest themselves, among others, in larger amplitudes of the isotherm-time series, in the formation and propagation of an internal surge and in the generation of an internal seiche, which, however, must be regarded as small in comparison to the original amplitudes of the isotherm

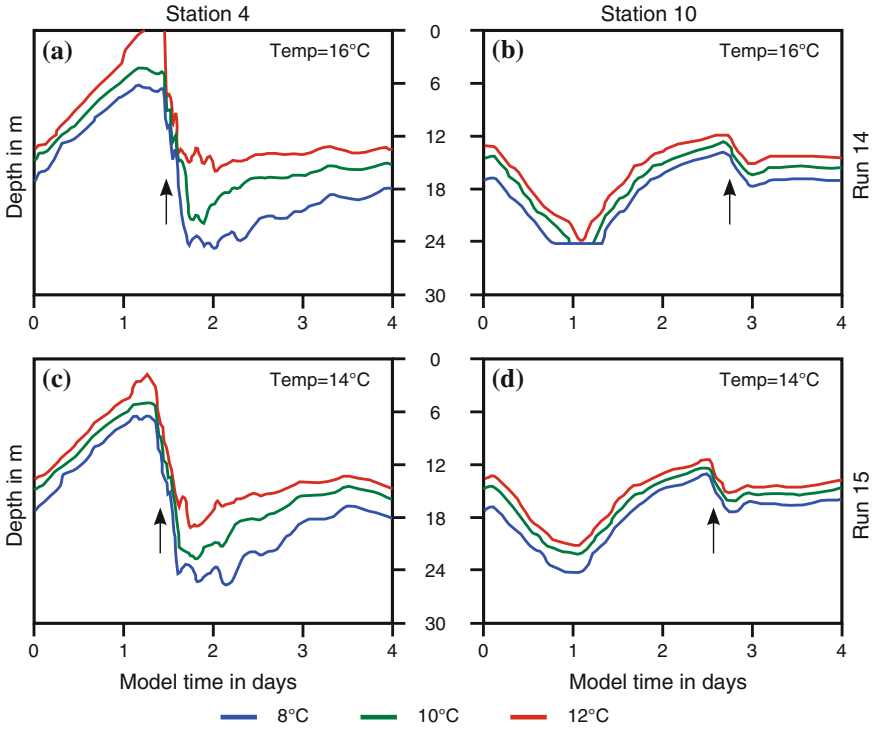


Fig. 24.19 Time series of the isotherm depths at station 4 (*left column*) and 10 (*right column*) for the 18-layer model with BENNETT's areal viscosity and epilimnion temperature of 16 °C (*top row*) and 14 °C (*bottom row*), from [19]. © Versuchsanstalt für Wasserbau, Hydrologie und Glaziologie an der ETH Zürich, reproduced with permission

depths. Not having details on the exact initial velocity and temperature distributions, the initial conditions have been chosen as a state of rest for the velocity and a horizontally uniform temperature distribution according to the 18-layer model of Table 24.2 with the exception of the top layer (0–4 m), in which $T = 20\,°\mathrm{C}$ was selected. A justification is given below. During the days of simulation this lack of exact knowledge of initial conditions alone must yield differences between the observed and computed field quantities.

For this, the relatively realistic conditions of Run 11 with 18 layers were used, however, with a quadratic grid of 375 m side length. This new choice of horizontal discretization allows a relatively reliable computation of the current distribution in the lake without the excessively large computational times that were involved with the 18-layer model and 250 m small net. The 20 °C initial epilimnion temperature was selected in the top layer for the motion out of a state of rest because the 19 °C choice is appropriate for a profile measured immediately after the storm, when turbulent mixing by the storm has already somewhat reduced the epilimnion temperature. The

time series of the measured temperature profiles show in the upper most layers indeed a temperature drop of this magnitude.

The wind shear stresses in the three meteorological stations 4, 6 and 11 have been computed by using time series of wind speeds measured 3 m above the lake surface according to Eq. (24.27). Because the direction of the wind at these stations with a 10 min measuring interval could not be reliably obtained, the wind shear tractions were averaged over 60 min intervals. Moreover, the distribution of the wind shear tractions at the lake surface was determined by interpolation using the wind shear tractions of these three stations.[8] Figure 24.20 displays the wind shear traction distribution just above the free surface of Lake Zurich at the time of the storm peak (12 September 1978, ca 20:00 GMT) for the wind event displayed in the top panel of Fig. 24.10. Because the wind is the only driving element in the model and of short duration, the heat input by radiation and by sensible and latent heat at the free surface and, correspondingly by the geothermal heat at the basal surface can be ignored.

The computations were started at midnight (00:00 GMT) of 8 September, three days before the onset of the storm and continued until 17 September, 9 days later. The computed time series of the 8-, 10- and 12 °C-isotherm depths at the stations 4, 6, 9, 10, 11, 12 are displayed in Fig. 24.21. Qualitatively, the computed isotherms are similar to those measured. Moderately strong winds of 5 ms^{-1} strength from south-west on the first day (8 September) triggered on the following day (9. September) an internal surge with amplitudes of the 8- to 12 °C-isotherms, which reached at station 4 several meters, but were much smaller at the other stations. The south-west storm started at the end of the third day (11 September) and was at that time in near counter phase to the motion in the lake. This led in the model as well as in Nature to a relatively rapid return of the motion and an equally rapid fall of the isotherms. This fall of the isotherms arises at the four stations 9, 10, 11, 12 in the eastern portion of the basin (i.e., down-wind) simultaneously with the peak of the wind shear traction at the beginning of the fifth day (12 September). About 8 h later, the internal front (shown in Fig. 24.21 by the arrows) reaches station 6 and after further 7 h station 4. At least with regard to this internal surge the observed isotherm depths behave quite similarly; in particular, a reversal of the direction of the internal front at the north-west lake end arises in Nature as well as in the model. Its speed of propagation in the measured isotherm depths is, however, faster, and the down fall of the isotherms at any station at the instant of the passage of the front is more abrupt and stronger in Nature than in the model, in particular for the first return at Zurich. Before the

[8] If f_i is the value of f at point i and f_α ($\alpha = 1, 2, \ldots$) are the values of f at the measuring stations α, then we choose

$$f_i = \sum_{\alpha=1}^{3} w_\alpha f_\alpha \quad \text{(for three stations)}.$$

w_α are weighting functions, which are chosen as follows:

$$w_\alpha = \exp\left[\left(d_\alpha / d_{\alpha_0}\right)^{-2}\right], \qquad d_\alpha = \sqrt{(x - x_\alpha)^2 + (y - y_\alpha)^2},$$

where d_{α_0} are constants with dimension [m].

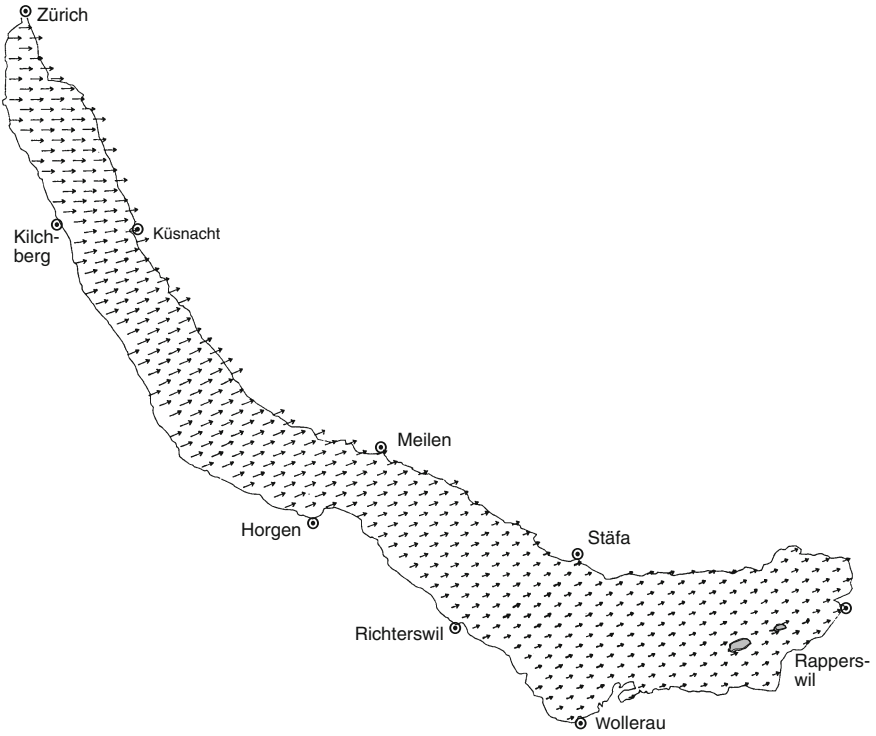


Fig. 24.20 Distribution of the wind shear tractions immediately above the free surface of Lake Zurich at the time of the peak of the storm (12. September 1978, ca. 20.00 GMT), computed for the wind event shown in Fig. 24.11). The grid size corresponds to wind shear traction of 5.6 Pa, from [19]. © Versuchsanstalt für Wasserbau, Hydrologie und Glaziologie an der ETH Zürich, reproduced with permission

front passes stations 9, 10, 11, 12 the time series of the isotherms rise in Nature and in the model relatively slowly to a 'large hump'. Its arrival agrees with the point of culmination and the immediate ensuing fall of the isotherms. The slope of this flank is, however, less steep than in Nature. After the passage of the front, a moderately strong stimulation of the fundamental internal seiche sets in, but the clear return of the internal front in Nature is not conspicuously recognizable in the model.

In the test runs the internal front was accompanied by a short but acutes pulse of the vertical velocities; it was certainly caused by this strong down fall of the isotherms. This peak or pulse arose first at station 4, but propagated along the lake eastward to Rapperswil. In the model it was accompanied by pulsations of the vertical velocities, which led to the numerical difficulties, were several times mentioned already and could only be reduced by a smoothing of the horizontal velocity field. Such a downward wave, though less conspicuous, can also be seen in the computed time series of the vertical velocities of the last run, which was performed for the actual (hourly averaged) wind event. This wave signal in Fig. 24.22, marked by arrows, is initially hidden behind the pulsations, which probably has physical as well

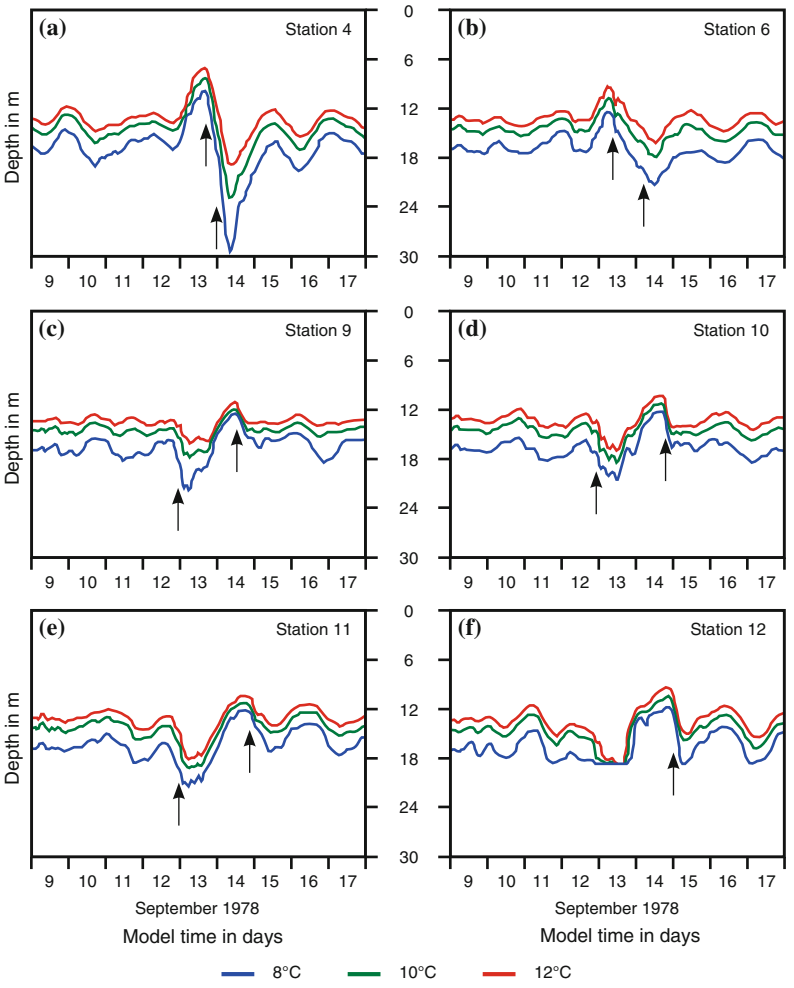


Fig. 24.21 Computed 8-, 10- and 12 °C-isotherm-time series at the stations 4, 6, 9, 10, 11, 12 for the wind event of Fig. 24.11. *Arrows* mark the times when the internal surge generated by the wind passes the station. Computations have been started on 8 September 1978, 00:00 GMT and have been continued for 9 days until 17. September 1978, 24:00 GMT, from [19]. © Versuchsanstalt für Wasserbau, Hydrologie und Glaziologie an der ETH Zürich, reproduced with permission

as numerical causes. However, the character of this wave is considerably different from that of the test runs. As in Nature, it is generated at the south-eastern lake and propagates towards Zurich where its return follows. Initially this down stroke wave is rather sharp, but not as large as in the test runs and most likely neither as large as in Nature; this is so, because the computed falls in the isotherm depths are smaller than those observed. In this regard the cause for the unsatisfactory performance of the model is perhaps the temporal smoothing of the wind, which was necessary because of

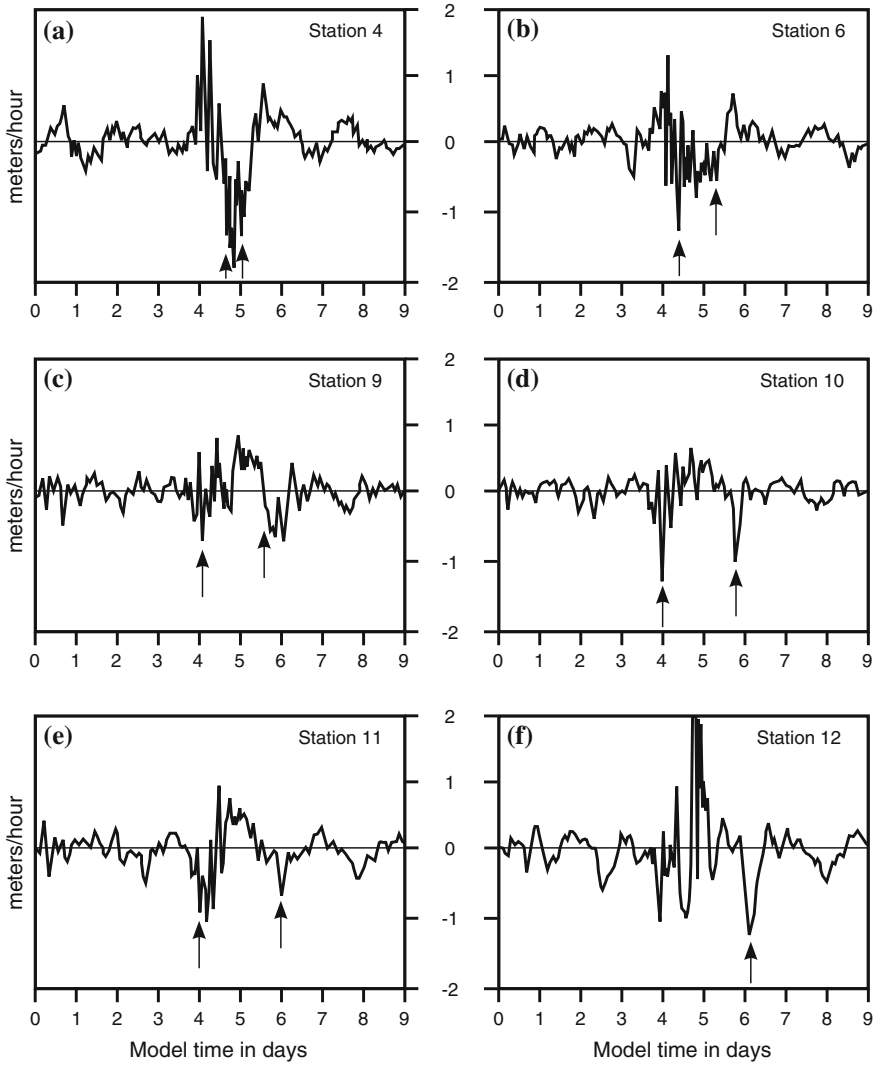


Fig. 24.22 Time series of the vertical velocity at the stations 4, 6, 9, 10, 11, 12 for the wind event of Fig. 24.12. *Arrows* mark the times when the internal surge generated by the wind passes the station. Computations have been started on 8 September 1978, 00:00 GMT and have been continued for 9 days until 17 September 1978, 24:00 GMT, [19]. © Versuchsanstalt für Wasserbau, Hydrologie und Glaziologie an der ETH Zürich, reproduced with permission

the inadequacies of the measured orientation of the wind.[9] In the development of the short-lived down stroke wave, the high-frequency pulsations, which were observed

[9] Because the *modulus* of the wind was computed by averaging the 'windweg', its experimental determination is more accurate than the determination of the *direction* (which is an instant quantity). It may therefore be better to use the non-averaged modulus and to average the direction

in the test runs, play certainly also a role. In spite of this, the model predicted the formation of the internal surge correctly.

The 'reflection' of the front at Zurich is equally correctly reproduced by the model. The isotherm down stroke at station 4 after this reflection possesses, however, a broader and flatter wave form than in nature and, later, can hardly be recognized at stations 6 and 9. Only at stations 10 and 11 this wave is again a bit more prominent. That the down fall of the isotherm depths in the model computations takes place only considerably slower than in the observations can also be traced back to the broadening of this down fall regime of the isotherms. Shoaling of the internal surge takes also place in Nature.

The above claims are obtained by a relatively cumbersome comparison of the computed isotherm-depth-time series, subject to the real applied wind, and those of the measurements, see Fig. 24.11. To facilitate this comparison and in order to perform a more accurate comparison between model computations and the measurements in Nature, the computed and measured time series have been plotted in the same graphs in Figs. 24.23 and 24.24 for the 8–14 °C isotherm-depths at the stations 4, 6, 9, 10, 11. The time series start on 8 September and extend to 15 September 1978. In the first days differences between measured and computed isotherm depths are discernible; they can be traced back to the different initial conditions. Generally, the measured isotherm depths lay above those computed; reason for this is most likely an inaccurate temperature distribution at the beginning of the model computations. In Nature the structure of the temperature in the vicinity of the different stations is influenced by the local conditions, which were not, and could not, be taken into account in the model because of lack of data. On the other hand, such local effects should not affect the global response of the water motion in the entire lake.

During the four days before the storm the measured isotherm-depth-time series indicate a far stronger generation of the first-mode internal seiche than is seen in the results of the model computations; this may be so, because the moderately strong wind on 8/9 September re-enforced an internal oscillation, which already existed before. Initially, the modeled internal seiche is in near counter phase (phase shift 180°) to that in Nature. This phase shift continues for a few days and only disappears with the appearance of the strong wind on the fourth day (11 Sept.). Owing to this wind the epilimnion is subject to a strong mixing, which leads to a small temperature reduction in the upper most layer and simultaneously to a corresponding small temperature increase in the upper metalimnion. This explains why the measured isotherms fall. At this time the measured and modeled isotherm depths are comparable, however, in the model this mixing in the upper most layer could not be properly reproduced. The reason is that the numerical values of the thermal diffusivity close to the thermocline are of the order of magnitude of the physical thermal diffusivity, so that they considerably affect the variation of the temperature. For this reason the explicit physical vertical diffusivity was set to zero, even though during the storm this physical diffusion in the epilimnion is probably far greater than the numerical diffusion.

With the onset of the strong wind at the end of the fourth day (11 Sept.) a relatively rapid isotherm downfall occurs both in the model and in Nature. Because of the

stronger stimulation of the internal seiche in Nature than in the model, this isotherm downfall is more conspicuous in Nature than in the model. However, the instant when this internal surge reaches stations 10 and 11 (this is at the end of the fourth day, 11 Sept.) is currently predicted by the model. As in Nature, the large and sudden downfall is followed by an episode, during which relatively short-periodic oscillations are superposed on the global motion; with time these oscillations experience, however, a phase shift. Later, at station 9 the internal front is seen as a double downfall. The size and the time of this fall is approximately correctly predicted by the model, but the inclination of the time series in the model is a bit too flat. However, the isotherms in Nature drop at lower depths, fall somewhat more than at upper depths, and the arrival of the internal front at station 6 is in the model about two hours too early. Furthermore, the measured isotherms fall after the passage of the front quicker to lower depths than those computed. Afterwards, the measured isotherms remain relatively flat whereas the computed ones continue to fall; moreover, in the model the front reaches station 4 too early and the slopes of the isotherm depths after the passage of the front are again too small.

After the reflection of the internal wave near Zurich at the end of the fifth day (12 Sept.) the downfall of the isotherms at station 4 is far more rapid in Nature than in the model, whereas an approximate determination of the passage of the front is possible, this is much more difficult for the modeled isotherm-depth-time series because the slopes of the measured isotherms are much less inclined than in Nature. However, once the front has further moved, the computed and measured isotherm-depth-time series at station 4 are again in better coincidence. The formation of the fundamental internal seiche is recognizable in both time series groups, whose period can be estimated from each panel of Figs. 24.23 and 24.24 to be approximately 44 h. The speed of propagation can equally be determined. Because the measured isotherm depths at station 6 are flat behind the front, but the computed ones still fall, the computed isotherm downfall is much smaller than in Nature. However, if the front has passed the station the second time, the isotherm-depth-time series of both groups are very similar to one another, compare station 4.

At station 9, the front of both model and nature is established immediately after a continuous rise of the isotherm depths. The subsequent down fall takes place in the model a few hours before the abrupt drop of the observed isotherms; this downward motion of the computed isotherms at the second passage of the surge is by far slower than for the measured isotherm depths. However, with growing time, this difference gets smaller. In stations 10 and 11 the situation is qualitatively very similar as in station 9. As in Nature, the computed isotherm depths after the second passage of the front are subject to a larger downfall in station 10 than station 11, an effect, which can be traced back to the influence of the CORIOLIS force. Moreover, the fundamental seiche after the second passage of the surge is in both, model and experiment, less disturbed in station 11 than in station 10.

The measurements indicate a third return of the internal surge, which, however, is no longer discernible in the computed isotherm-depth-time series. This front is particularly conspicuous at the 7th day (14 Sept.) in the isotherm depths of station 11; somewhat later, it can also be seen at station 4. This continued internal front

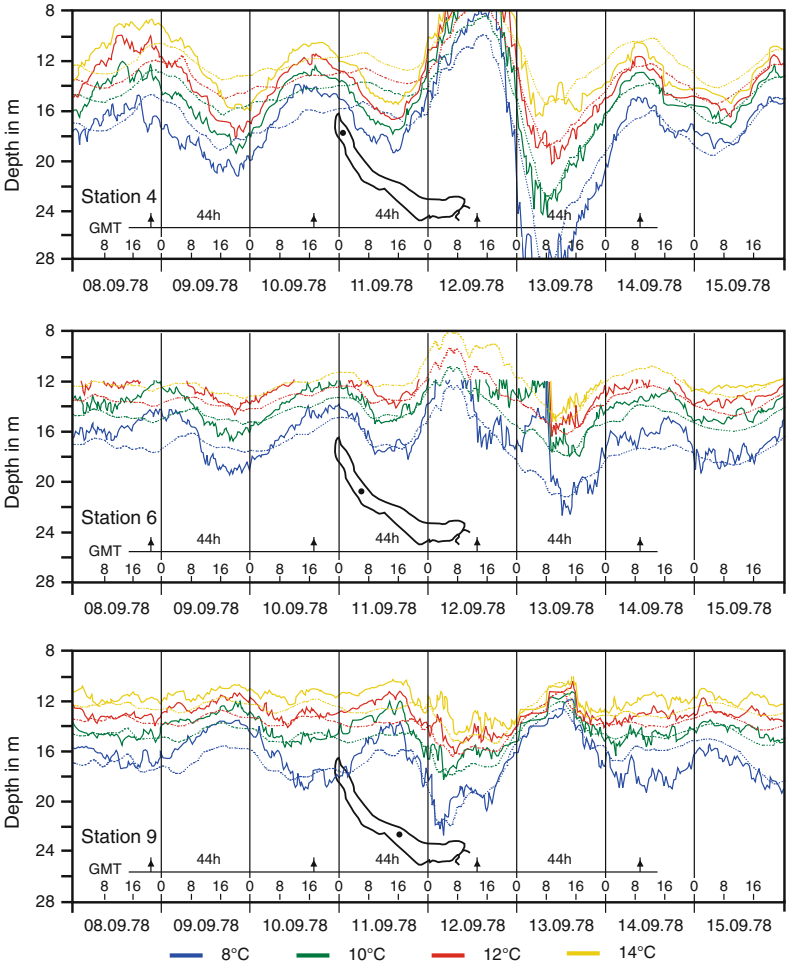


Fig. 24.23 Lake Zurich comparison of time series of the 8-, 10-, 12- and 14 °C-isotherm depths, obtained from measurements (*solid curves*) and model (*dotted*) at the stations 4, 6 and 9 from 8 September 00:00 GMT until 15 September, 24:00 GMT. The isotherm depths obtained from temperature measurements were obtained with temperature recordings taken at 20 min intervals. Full triangles identify the 44 h period of the fundamental seiche and arrows mark the beginning of the calculated internal surge, which starts somewhat earlier than in nature. The measured isotherm depths are constructed from unfiltered temperature time series, from [19]. © Versuchsanstalt für Wasserbau, Hydrologie und Glaziologie an der ETH Zürich, reproduced with permission

obviously exerts its imprint on the measured isotherm depths which is smeared in the computations and actually only poorly reproduced.

A further comparison of the model output with observed data from Nature was focused on comparisons of computed horizontal velocities and measured counterparts, now at stations, where current meters were moored. In this comparison the

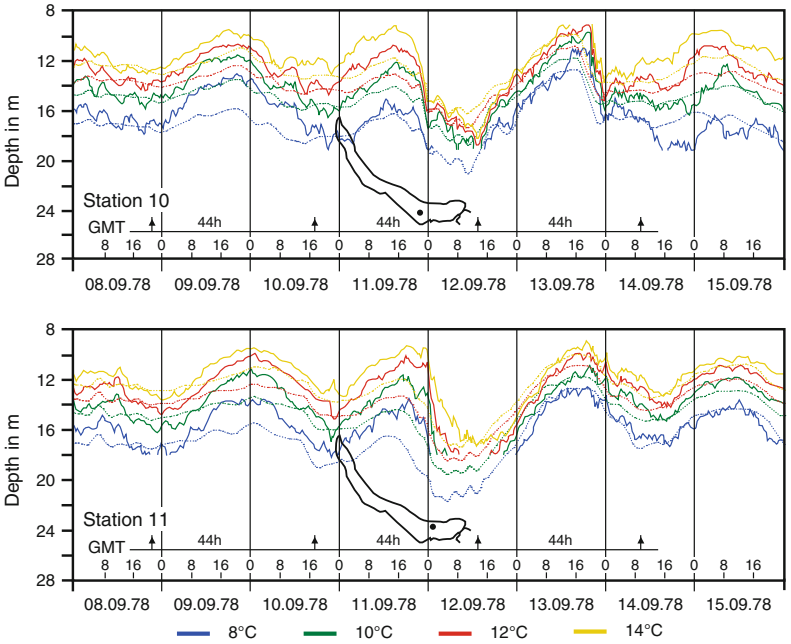


Fig. 24.24 Same as Fig. 24.23, but now for stations 10 and 11, [19]. © Versuchsanstalt für Wasserbau, Hydrologie und Glaziologie an der ETH Zürich, reproduced with permission

computed horizontal velocities in the third and fourth layers were depth averaged. They were compared with an estimation of the currents at 6 to 10 m depth. In order to smooth the short periodic pulsations, the measured horizontal velocities within this layer at stations 1, 4, 5, 6, 8, 10, 11, and 12 were averaged over 4 h. A comparison of the measurements with the computed velocity field is only reasonable, if a point measurement is representative for the entire layer at the 6-10 m depth, i.e., at times when no great shearing affects the currents. Time series of the computed horizontal velocities indicate, see [19], that large shearing of the horizontal velocities only arises within the epilimnion during the period of strong wind input. The exact position of this maximum shearing cannot be inferred from the velocities, because only a single current meter was moored within the epilimnion at all measuring stations of the 1978 field campaign.

OMAN [19] constructed plots of a comparison of the horizontal velocities at 18 time slices from 12 September 00: 00 GMT until 14. September 08:00 GMT at every 4 h. This obviously conceptually short but also elaborate study led him to conclude that, qualitatively, an analogous behavior of the measured and computed velocities can be identified with only loose agreement. However, a quantitative agreement between observed velocities and the averaged velocities between 6-10 m is only possible under strong winds which trigger strong advection within the lake. Figure 24.25 shows velocity plots from 12 September 08:00 GMT, computed as described above. The positions where a current meter was moored between 6 and 10 m are encircled.

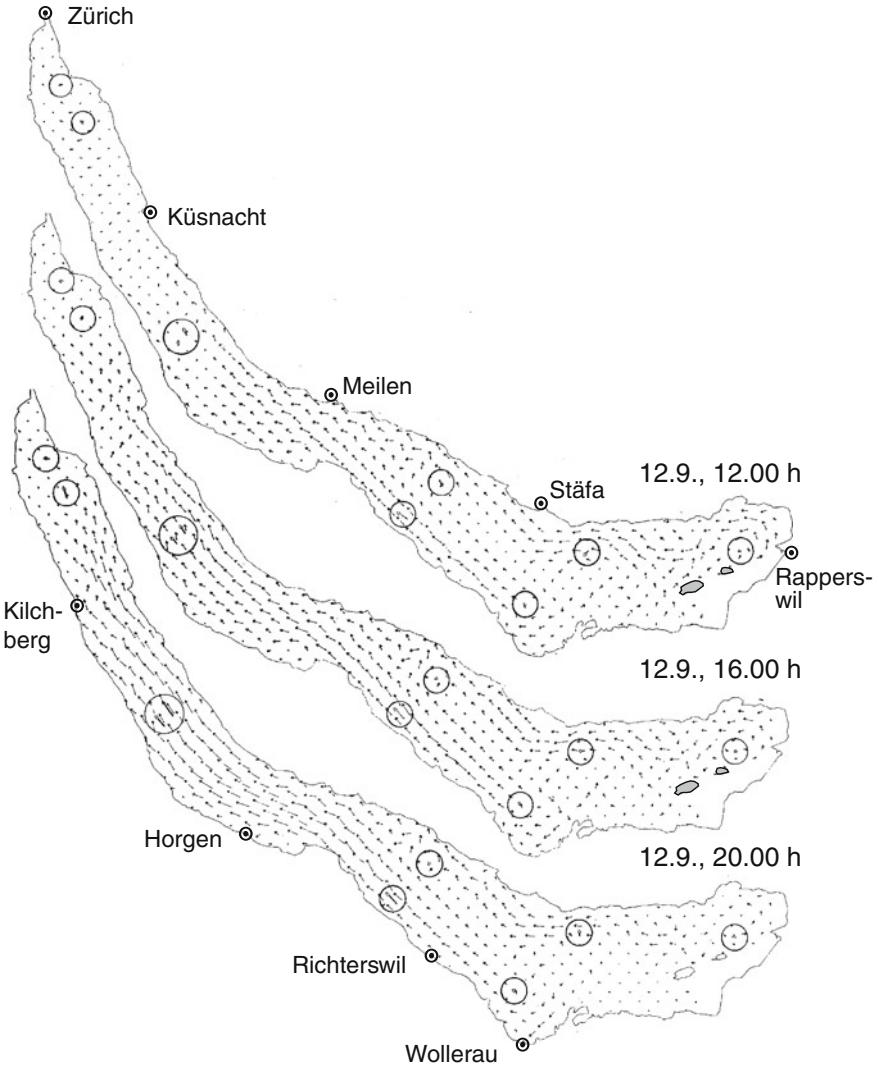


Fig. 24.25 Lake Zurich mean horizontal velocity field in 6–10 m depth for the episode from 12 September 1978, 12:00 GMT until 13 September 08:00 GMT. *Solid arrows* show the calculated current, *hollow arrows* 4 h averages of the measured current for the same times at the stations 1, 4, 5, 6, 8, 9, 10, 11, 12. *Arrows* with length corresponding to 375 m correspond to velocities of 15 m s^{-1}, from [19]. © Versuchsanstalt für Wasserbau, Hydrologie und Glaziologie an der ETH Zürich, reproduced with permission

OMAN concludes that 'the agreement between the measured current and the computed field is at all measuring stations fairly good', and these are the best results among all 18 cases that were explicitly explored.

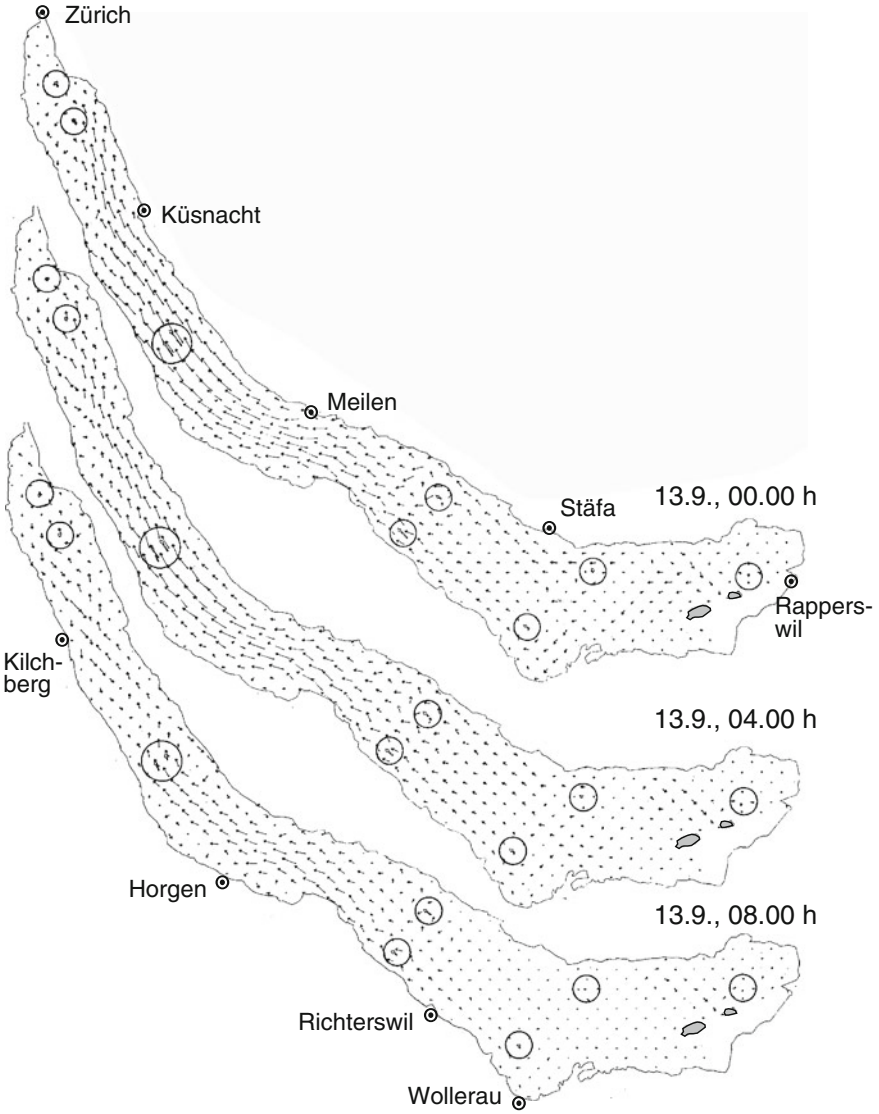


Fig. 24.25 (continued)

We add to this our own critical remark, that point measurements of velocities, when used for judging the accuracy of a numerical model require careful elaboration by taking averages of both the measured quantities and of the computed fields to the extent that commensurability of the averaged data and computed fields seems rather doubtful.

24.6 Discussions and Conclusion

The preceding comparison between the model computations and natural observations of the wind induced circulating motion and temperature variations in Lake Zurich subject to summer stratification suggest a better agreement of the two than was anticipated after the accumulated knowledge of the extensive test runs. In these it was recognized that numerical stability required smoothing of the horizontal velocity field and led to 'false' numerical diffusion of the temperature. However, because these two processes cause destruction of mechanical (kinetic and potential) energy and consequential suppression of the internal seiche response, the influence of these two terms was as far as possible constrained by use of the 'areal viscosity' of BENNETT and by application of the 'flux corrected' transport approach in the integration of the energy equation. In spite of this, the suppression of the internal seiche was bigger than expected, as the internal seiche had died out after a single oscillation. Instead, the linear theory suggests only a slow attenuation of the internal oscillations. By refined vertical discretization and simultaneous reduction of the vertical momentum exchange the internal seiche could much better be predicted than expected. The test runs also proved that the effects of the CORIOLIS force and the advection of momentum onto the internal seiche were recognizable in the results if not dominant. Their finite difference approximation, however, did not cause any difficulties.

The model was also capable to correctly predict the observed manifestation of the internal surge. The velocity of propagation of this surge—as that of the internal seiche—is, however, strongly influenced by the stratification of the lake water. In fact, in the first test runs, the internal surge was propagating too slowly, probably because of a too low equilibrium temperature used in the model. The origin of the internal front was a large, steep downfall, which is generated at the lower lake end at Zurich and then propagates towards Rapperswil; a return of this wave at Rapperswil could not be discerned in the test runs.

All test runs also demonstrated a too rapid attenuation of the internal seiches. Since the corresponding 'failure' of the model can probably be traced back to the false numerical diffusion of the temperature, the explicit physical vertical heat exchange coefficient was set to zero. Alternatively, it is clear for the computation with the true actual wind, that in the epilimnion during the peak of the storm, the physical exchange coefficient must be larger than the value used in the model. This leads in Nature to a mixing of the epilimnion, which was not correctly reproduced in the model. Similar is the situation with the diffusion in the vicinity of the thermocline. Here, the physical heat exchange coefficient nearly vanishes completely, whereas

the numerical diffusion reaches a maximum. Generally, the simple representation of the vertical turbulent momentum and heat exchange, which were used in the model, must be regarded as unsatisfactory. Massive improvements of turbulent closure seem to be the necessary approach for progress.

Given the experience with the test runs, the relative successful agreement between model and Nature for the factual wind scenario and the nearly perfect stimulation of the fundamental internal seiche during and after the storm is surprising (and pleasing), in particular since the linear theory would predict a multifold forth and back swing of the internal seiche. The cause of the suppression of this swing in the model and in Nature is not clear: destruction of energy by turbulent exchange or non-linear effects as e.g. the development of the internal surge are possible candidates, which would need deeper scrutiny. Such analyses could perhaps explain, why a pure stimulation of the internal seiche in the test runs did not occur.

Unfortunately, none of such ideas has been tried in the last approximately 30 years. In fact, the worldwide unique electronic data collection with simultaneous measurements of temperature by 12 thermistor chains and with a total of 40 current meters has not been preserved by those who were responsible in 1978 and the ensuing years. Paper versions of drawings do exist and may help a bit. However, the results in this chapter have clearly shown that validation of numerical models for mountainous lakes in general and Lake Zurich, in particular, require observations from synoptic whole lake field campaigns. Unfortunately, even though such global synoptic campaigns have been and are being performed, their focus is generally too narrow for validation of software of baroclinic circulation dynamics during wind action and its aftermaths.

References

1. Bennett, J.R.: A three-dimensional model for Lake Ontario summer circulation: Comparison with observations. *J. Phys. Oceanogr.*, **7**, 591–607 (1977)
2. Heaps, N.S. and Ramsbottom, A.E.: Wind effects in a narrow two-layered lake. *Phil. Trans. Royal Soc. London*, **A259**, 291–302 (1966)
3. Horn, W.: *Zürichsee 1978: Physikalisch-limnologoisches Messprogramm und Datensammlung*. Internal Report Nr. 50, Versuchsanstalt für Wasserbau. Hydrologie und Glaziologie an der Eidgenössischen Technischen Hochschule, Zürich. (1981)
4. Horn, W., Mortimer, C.H. and Schwab, D.J.: Wind-induced internal waves in the Lake of Zürich, observed and modeled. *Limnol. Oceanogr.*, **31**(6), 1230–1252 (1986)
5. Hutter, K.: Strömungsdynamische Untersuchungen im Zürich- und im Luganersee - Ein Vergleich von Feldmessungen mit Resultaten theoretischer Modelle. *Schweiz. Z. Hydrologie*, **45**(1), 101–144 (1983)
6. Hutter, K., Bucher, C. and Salavdè, G.: *Messungen von Wasserspiegelschwankungen mit Hilfe von Seiche Limnigraphen im Zürichsee*. Internal Report Nr. 57, Versuchsanstalt für Wasserbau. Hydrologie und Glaziologie an der Eidgenössischen Technischen Hochschule, Zürich. (1982)
7. Hutter, K., Raggio, G., Bucher, C. and Salvadè., G.: The surface seiches of Lake of Zürich. *Schweiz. Z. Hydrol.*, **44**(2), 423–454 (1982)

8. Hutter, K.: Mathematische Vorhersage von barotropen und baroklinen Prozessen im Zürich und Luganersee. *Vierteljahresschrift der Naturforschenden Gesellschaft in Zürich*, **129**(1), 51–92 (1984)
9. Hutter, K., Oman, G. and Ramming, G.:Windbedingte Strmungen des homogenen Zürichsees. *Mitteilung Nr 61 der Versuchsanstalt für Wasserbau, Hydrologie und Glaziologie an der ETH Zürich*, pp. 1–123 (1982)
10. Hutter, K.: (with contributions by Bäuerle, E., Salvadè, G., Spinedi, C. and Zamboni, F.: Large scale water movements in lakes. *Aquatic Sciences*, **53**, 100–135 (1991)
11. Hutter, K., Wang, Y. and Chubarenko, I.: *Physics of Lakes* Volume 1: *Foundation of the Mathematical and Physical Background*, Springer Verlag, Berlin etc., pp. 434 (2011)
12. Hutter, K., Wang, Y. and Chubarenko, I.: *Physics of Lakes* Volume 2: *Lakes as Oscillators*, Springer Verlag, Berlin etc., pp. 646 (2011)
13. Laska, M.: Characteristics and Modelling of physical limnology processes. *Mitteilung Nr 54 der Versuchsanstalt für Wasserbau, Hydrologie und Glaziologie an der ETH Zürich* (1981)
14. Leendertse, J.J., Alexander, R.C. and Liu, S.K.: *A three-dimensional model for Estuaries and Coastal Seas, Vol I: Principals of computation*. The Rand Corporation (1977)
15. Leendertse, J.J. and Liu, S.K.: *A three-dimensional model for Estuaries and Coastal Seas, Vol IV: Turbulent Energy Computations*. The Rand Corporation (1977)
16. Mortimer, C.H.: *Preliminary examination of temperature, current and wind records obtained in the 1978 Lake of Zürich field experiment*. Internal Report Nr. 53, Versuchsanstalt für Wasserbau. Hydrologie und Glaziologie an der Eidgenössischen Technischen Hochschule, Zürich (1982)
17. Mortimer, C.H. and Horn, W.: Internal wave dynamics and their implications for plankton biology in the Lake of Zürich. *Vierteljahresschrift der Naturforsch. Ges. Zürich*, **137**, 299–318 (1982)
18. Munk, W.H.: On the wind-driven ocean circulation. *J. Meteorol.*, **7**, 79 (1950)
19. Oman, G.: *Das Verhalten des geschichteten Zürichsees unter äusseren Windlasten - Resultate eines numerischen Modells*, Mitteilung Nr 60 der Versuchsanstalt für Wasserbau, Hydrologie und Glaziologie an der ETH Zürich, pp. 1–185 (1982)
20. Schwab, D.: *Determination of wind stress from water level fluctuations*. Ph.D. thesis, University of Michigan, Ann Arbor (1981)
21. Simons, T.J.: Development of three-dimensional numerical models of Great Lakes. *Sci. Series No 12, Inland Waters Directorate*, Canada, Centre of Inland Waters, Burlington, Ontario. (1973)
22. Simons, T.J.: Verification of Numerical Models of Lake Ontario, Part I: Circulation in Spring and early Summer. *J. Phys. Oceanogr.*, **4**, 507–523 (1974)
23. Simons, T.J.: Verification of Numerical Models of Lake Ontario, Part II: Stratified Circulations and temperature changes. *J. Phys. Oceanogr*., **5**, 98–110 (1975)
24. Simons, T.J.: Verification of Numerical Models of Lake Ontario, Part III: Long term heat transports *J. Phys. Oceanogr*., **6**, 372–378 (1976)
25. Simons, T.J.: Circulation models of lakes and inland seas. *Canadian Bulletin of Fisheries and Aquatic Sciences*, Bulletin **203**, Ottawa
26. Sydor, M. and Oman, G.J.: Effects of Nemadji Runoff on Lake Superior. *Final Report, U.S. E.P.A. Grant R-005286-01*, Department of Physics, University of Minesota, Duluth, 197 pp. (1977)
27. Taylor, G.I.: Tidal friction in the Irish Sea. *Phil. Trans. Royal. Soc. London*, **A220** pp. 1–33 (1919)
28. Wang, Y.:*Windgetriebene Strömungen in einem Rechteckbecken und im Bodensee*. Ph. D. Dissertation, Technische Hochschule, Darmstadt (1995)

http://www.springer.com/978-3-319-00472-3

Physics of Lakes
Volume 3: Methods of Understanding Lakes as Components of the Geophysical Environment
Hutter, K.; Chubarenko, I.P.; Yongqi, W.
2014, LXVI, 605 p. 237 illus., 70 illus. in color.,
Hardcover
ISBN: 978-3-319-00472-3